UCSF
UC San Francisco Previously Published Works

Title

Phenotypic discovery of GABAA receptor-mediated general anesthetics with analgesic activity

Permalink

https://escholarship.org/uc/item/33m1546s

Journal

Nature Communications

ISSN

2041-1723

Authors

McCarroll, Matthew N
Weinrich, Jarret AP
Marinas, Alyssa H
et al.

Publication Date

2026-11-16

DOI

10.1038/s41467-026-79384-x

Peer reviewed

eScholarship.org Powered by the California Digital Library
University of California

nature communications

Article | Article in Press

https://doi.org/10.1038/s41467-026-79384-x

Phenotypic discovery of $GABA_A$ receptor-mediated general anesthetics with analgesic activity

Received: 11 December 2025

Accepted: 15 October 2026

Published online: 16 November 2026

Check for updates

Matthew N. McCarroll[1,10] ✉, Jarret A. P. Weinrich[2,3,10], Alyssa H. Marinas[4,10], Amanda Dombroski[5], Lain X. Pierce[1], Xilin Gu[1], Megan J. Larmore[4], Jinfeng Teng[4], Elizabeth J. Sisko[1], Christopher Andolina[3], Ricardo Da Luz[1], Ralph Zhang[1], Jack C. Taylor[6], Douglas Myers-Turnbull[1], Cole Helsell[1], Amanda Carbajal[6], Reid Kinser[6], Madison Jewell[3], Karnika Bhardwaj[3], Sian Rodriguez-Rosado[3], Israr Ali[3], Jennifer Deuis[7], Asa Andersson[7], Bruce P. Bean[8], Irina Vetter[7], Timofey Glinin[9], Sanziana A. Roman[9], James Koh[9], Michael P. Bokoch[2], Brian K. Shoichet[1], David Kokel[6], Ryan E. Hibbs[4] ✉, Allan I. Basbaum[3] ✉ & Jason K. Sello[1] ✉

General anesthetics are essential for invasive medical procedures; however, there remains a need for safer agents. Using a bespoke 96-well-plate format platform enabling high-throughput imaging of larval zebrafish behavior, we screen 12,000 compounds and identify an isoxazole chemotype that phenocopies the intravenous anesthetics etomidate and propofol. Its optimization via medicinal chemistry yields an anesthetic that we call nidradine. This anesthetic is efficacious in both zebrafish and mice and lacks the problematic adrenal suppression characteristic of etomidate. Mechanistic studies using electrophysiology and structural biology reveal that nidradine, like etomidate and propofol, is a positive allosteric modulator of the $GABA_A$ receptor. Remarkably, behavioral assays in mice demonstrate that nidradine differs from most general anesthetics in that it also produces analgesia at sub-sedative doses.

Despite their widespread use[1], general anesthetics have a suboptimal therapeutic profile. The most commonly used intravenous general anesthetic, propofol, causes unfavorable hemodynamics and respiratory depression, while etomidate causes adrenal suppression that is linked to increased mortality[2,3]. The $GABA_A$ receptor is the major target of many general anesthetics[4–6]. It is a ligand-gated ion channel assembled as a pentamer of homologous subunits. The existence of 19 different receptor subunits in humans underlies an incredible diversity of $GABA_A$ receptors having distinct signaling properties and pharmacology[7]. The most abundant subtype in the human brain comprises α1, β2, and γ2 subunits[8,9]. $GABA_A$ receptor activation by GABA or exogenous molecules triggers opening of an intrinsic anion channel, which in most cases results in intracellular chloride conductance, dampening neuronal excitability. Notably,

[1]Department of Pharmaceutical Chemistry, University of California, San Francisco, CA, USA. [2]Department of Anesthesia and Perioperative Care, University of California, San Francisco, CA, USA. [3]Department of Anatomy, University of California, San Francisco, CA, USA. [4]Department of Neurobiology, University of California, San Diego, CA, USA. [5]Department of Chemistry, Brown University, Providence, RI, USA. [6]Institute for Neurodegenerative Diseases, University of California, San Francisco, CA, USA. [7]Institute for Molecule Bioscience, University of Queensland, St Lucia, QLD, Australia. [8]Blavatnik Institute of Neurobiology, Harvard Medical School, Boston, MA, USA. [9]Department of Surgery, University of California San Francisco, San Francisco, CA, USA. [10]These authors contributed equally: Matthew N. McCarroll, Jarret A. P. Weinrich, Alyssa H. Marinas.
✉e-mail: matthew.mccarroll@ucsf.edu; jason.sello@ucsf.edu; allan.basbaum@ucsf.edu; rehibbs@ucsd.edu

common intravenous anesthetics that act on the $GABA_A$ receptor, including etomidate and propofol, lack analgesic properties[10,11], necessitating additional pain management measures, often via opioids[12].

The discovery and development of anesthetics remains challenging, given that anesthesia must be assessed in mammals via expensive and low-throughput experiments. In the past decade, aquatic vertebrates have emerged as an alternative to mammals in the discovery of neuroactive compounds. Indeed, early zebrafish screens established reproducible behavioral barcodes (i.e., phenotypes) that predict mechanism and revealed psychoactive scaffolds[13,14]. The fact that immersion dosing in these animals rapidly attains near-steady-state exposure in vivo facilitates chemical screens[15]. In neuroactive discovery, a focused zebrafish larval photomotor-response screen (~374 compounds) identified reversible anesthetics like sedative–hypnotics with activity spanning $GABA_A$, neuronal nicotinic, and NMDA receptors[15], illustrating that target-agnostic phenotypic assays can identify hits, including those that act through multiple targets. Studies in zebrafish have even yielded propofol antagonists, fluorinated analogs that reverse propofol anesthesia, underscoring the capacity of these models to uncover both agonists and antagonists[16].

We recently developed a screening approach that uses larval zebrafish, in which anesthetics produce rich behavioral fingerprints beyond simple immobility, namely measurable transient hyperexcitability or altered responses to specific stimuli[17]. By capturing these patterns, behavioral screening in zebrafish is amenable to high-throughput approaches for discovering anesthetic drugs. Like other vertebrates, zebrafish exhibit a complex repertoire of behaviors, yet their central nervous system is far simpler in architecture[18]. Because zebrafish larvae are small enough to fit in 96-well plates and are readily dosed with compounds dissolved directly in the water, it is possible to do high-throughput screens of thousands of compounds. Indeed, zebrafish have been used to screen and identify pharmacological compounds, some of which have shown promising translational potential in mammalian models and have progressed to clinical trials (e.g., clemizole and lorcaserin for Dravet syndrome; and the mechanosensory hair-cell otoprotectant ORC-13661)[19–21]. Importantly, the $GABA_A$ receptor gene family is highly conserved in zebrafish. Its genome contains at least 23 $GABA_A$ receptor subunits, including orthologs of all mammalian subunits, except θ and ε, and an additional subunit β4[22]. Like mammals, the zebrafish α subfamily is the largest and most diverse of the subfamilies.

Here, we report the execution of a high-throughput behavioral chemical screen in larval zebrafish that is predictive of general anesthetic activity. The screening hits that were also active in a secondary anesthesia screen in adult zebrafish proved to be efficacious in mice. Among them was an isoxazole whose analogs retained potent and reversible anesthetic effects. Medicinal chemistry efforts on the isoxazole scaffold yielded a lead compound that we named nidradine. Biophysical experiments revealed that nidradine potentiates $GABA_A$ receptor function and shares a binding site with known anesthetics, including etomidate and propofol. However, compared to $GABA_A$ modulating anesthetics, nidradine not only exerted enhanced surgical anesthesia but also exhibited analgesic activity.

Results

Discovery of anesthetics in zebrafish by phenocopying known anesthetics

To investigate the behavioral modifications induced by intravenous anesthetics in fish, we used a suite of automated behavioral assays tailored to distinguish between a diverse array of neuroactive substances[17]. The methodology incorporated a variety of acoustic and visual stimuli to detect substances that either decrease motor activity or increase startle responses to low-intensity acoustic signals. We previously reported that etomidate and propofol, which act through $GABA_A$ receptors, selectively provoke enhanced acoustic startle responses (eASRs) to low-intensity solenoid tap stimuli, but not to other sensory stimuli (Fig. 1a)[17]. Here, we screened 12,000 structurally diverse compounds from a ChemBridge DIVERSet library at 30 μM in larval zebrafish and examined their phenotypic similarity to the behavioral profile of etomidate (Fig. 1b). Sixty-nine compounds phenocopied etomidate and were designated as primary hits (refer to Supplementary Table 1).

We next categorized these hits by structural similarity and identified 22 distinct clusters (Supplementary Fig. 1, Supplementary Table 1). Certain clusters contained compounds having well-known pharmacophores. For example, Cluster 4 is enriched for piperidine–carbonyl scaffolds, a well-recognized CNS-active motif that includes local anesthetics (bupivacaine and ropivacaine). Cluster 17 was enriched for 8 scaffolds sharing an isoxazole (Supplementary Table 1), which is a bioactive and CNS-privileged heterocycle found in both synthetic and natural neuroactive molecules[23]. From the 69 primary hits, we selected 29 compounds representing the 22 chemoinformatic clusters for further testing (Supplementary Table 2). We conducted dose response trials and confirmed that 28 of the 29 recapitulated the eASR phenotype (Fig. 1c, Supplementary Fig. 2 and Supplementary Table 2), validating the reliability of the primary behavioral screen.

As age-dependent neuropharmacology and pharmacokinetics can influence drug responses[24–26], we next asked whether the anesthetized adult zebrafish. Because compounds identified in larval zebrafish do not always reproduce comparable anesthetic phenotypes in adult animals, potentially due to differences in compound distribution and brain penetration, we incorporated an adult zebrafish assay as a secondary screen to prioritize compounds with improved translational potential. Our analysis was based on observations that etomidate reliably produces behavioral endpoints of the hypnotic component of general anesthesia (i.e., ability to produce loss of responsiveness), namely loss of righting reflex (LoRR) and immobility in adult fish (Fig. 1d, Supplementary Movie 1). Accordingly, we used immobility as an endpoint for a secondary screen, in which adult zebrafish were treated with each of the 29 primary screening hits at 50 μM (Fig. 1d). We identified five compounds that induced robust anesthesia (Fig. 1d); among them, we prioritized compound 9232649 (MM01) since it has a structure that does not have clear major pharmacological liabilities and is amenable to the syntheses of analogs in a medicinal chemistry campaign.

Optimization of candidate chemotypes and anesthetic validation in mice

Given the favorable phenotypic and chemical properties of the oxazole carboxamide hit, MM01, we conducted a structure-based analog search and identified 70 commercially available compounds having >70% similarity to the parent molecule (Supplementary Table 3). Commercially available analogs were identified using the supplier's chemical similarity search tool (Chembridge). From the resulting hits, we selected compounds spanning a range of structural modifications, including both substituent changes and related scaffold variations, to broadly sample the chemical space surrounding the parent molecule. Compounds were prioritized for purchase and evaluation by calculating the Tanimoto similarity scores and performing hierarchical clustering (Fig. 2a). This analysis revealed 8 distinct structural clusters, and we selected 1 or more representative analogs from each cluster for a total of 13 analogs (Supplementary Table 3 and Supplementary Fig. 3).

From this analog-by-catalog screen, we identified 2 isoxazolecarboxamides [9267615 (MM02) and 9203415 (MM03)] that produced robust LoRR in adult zebrafish. Further characterization confirmed that these isoxazolecarboxamides were effective at

https://doi.org/10.1038/s41467-026-79384-x

sedating both larval and adult zebrafish (Fig. 2b, c). Based on these results, we initiated the synthesis of additional analogs to probe structure-activity relationships. Having affirmed the essentiality of the isoxazole carboxamide scaffold, we executed the syntheses of analogs from structurally diverse building blocks, including various cyclic and acyclic amines and isoxazole carboxylic acids having many different substituted aryl moieties at C2 in hopes of exploring the broadest range of chemical space. We did not use structure-guided design, but rather we focused on structural diversity and the exclusion of pharmacologically problematic moieties in our syntheses of analogs. In total, we synthesized 28 analogs within the oxazole and isoxazole chemical space (Fig. 2d, Supplementary Fig. 4 and Supplementary Table 4) and evaluated their behavioral effects in both larval and adult zebrafish (Fig. 2e, f). From this set of compounds, we identified 3 analogs that produced clear LoRR phenotypes in adults (Fig. 2g) and were soluble in aqueous media. Based on potency, solubility, and behavioral consistency, two of these were selected for further testing (Fig. 2f, chemical structures shown).

Next, we assessed the compounds for general anesthetic activity in mice. To assess for both the presence of a general anesthetic effect and dosing that produces LORR in 50% of trials (i.e., the ED_{50}), we used Dixon's up-down method[27]. IP injections of the parent molecule MM01, two of the analogs by catalog hits, and the two optimized analogs all produced LoRR in mice, indicating anesthetic properties (Fig. 2h). The synthetic analog AD-7-219 (nidradine) was the most easily dissolved in a vehicle known to be tolerated in mice (11% kolliphor EL/1.5% ethanol in saline). Pharmacokinetic analysis by LC–MS/MS after IP injection of nidradine in mice demonstrated that the compound distributed to the plasma and brain, consistent with a CNS-mediated general anesthetic action (Supplementary Fig. 5). In line with the pharmacokinetic data, time to onset of LORR is longer in mice injected with nidradine versus etomidate, but duration of effect is similar (Supplementary Fig. 6). Telemetric recordings of mouse physiology demonstrate that nidradine has similar maximum hemodynamic effects to etomidate, yet with extended duration of effect (Supplementary Fig. 7), likely due to differences between the

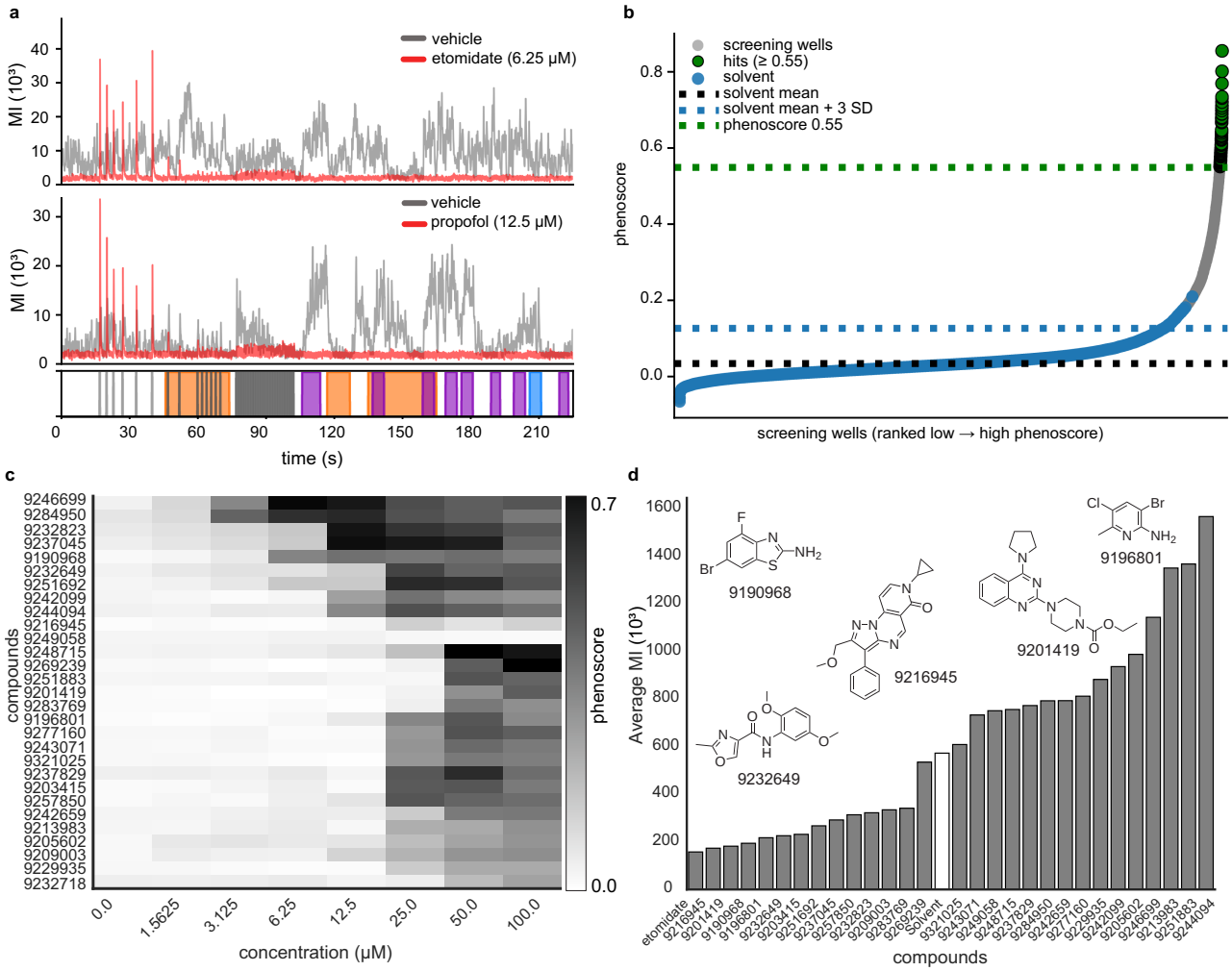


Fig. 1 | High-throughput behavioral screening identifies anesthesia phenocopy molecules in zebrafish. a Time-series behavioral profiles (motion index, MI; *y*-axis) of larval zebrafish during a multi-stimulus battery delivered at defined time points (*x*-axis). The stimulus track below marks timing: gray bars = solenoid taps; orange/blue/purple = visible-light stimuli. Traces show vehicle (gray) and anesthetic dosing: etomidate (red, top) and propofol (red, bottom). $n = 4$–12 wells per condition; 8 larvae per well. **b** Rank-ordered scatter of phenoscores (*y*-axis) across all screened wells (*x*-axis, sorted low–high). Dosing of wells is 30 μM. Dotted lines mark the vehicle (solvent) mean, vehicle mean + 3 SD, and the pre-specified hit threshold (phenoscore = 0.55), with hit wells denoted in green and vehicle noted in blue. **c** Dose–response heatmap for 29 retest compounds (rows), concentration is in μM. Each cell shows the mean phenoscore (color bar) across $n = 3$ wells at the indicated concentrations (columns); 0.0 denotes on-plate vehicle controls. **d** Adult zebrafish validation. Mean motion index (MI) per compound for the retest set; lower MI indicates reduced locomotor activity. Etomidate is the positive control; vehicle (solvent, white bar) is the negative control. Labeled structures of the five strongest adult hits are shown. Source data are provided as a Source Data file.

pharmacokinetic profiles of nidradine versus etomidate[28]. Importantly, nidradine did not cause the problematic inhibition of cortisol biosynthesis underlying adrenal suppression like etomidate (Supplementary Fig. 8) and human ex vivo tissue samples (Supplementary Fig. 9).

Nidradine potentiates the $GABA_A$ receptor through a membrane site

As nidradine was efficacious in inducing anesthesia in both fish and mice in a manner comparable to etomidate, we selected it for detailed mechanistic analysis. Many general anesthetics, including etomidate, propofol, and barbiturates, act by potentiating the activity of the $GABA_A$ receptor, which led us to ask whether nidradine acted via the same target and mechanism. This prediction was further strengthened by our recent findings that most phenocopiers of etomidate from smaller behavioral screens in larval zebrafish screens are positive allosteric modulators of the $GABA_A$ receptors[29]. On these grounds, we tested the activity of nidradine on the $GABA_A$ receptor in whole-cell patch-clamp electrophysiology experiments on HEK cells expressing the α1β2γ2 subtype of the receptor; this subunit assembly is the most abundant in the human brain and is known to be modulated by the general anesthetics mentioned above. We used S-nidradine, as this enantiomer was most active in both fish and mice (Supplementary Fig. 10).

We began by testing the activity of S-nidradine on the $GABA_A$ receptor in the absence and presence of GABA. We found that S-nidradine has both positive allosteric modulator (PAM) and allosteric agonist activities. At lower concentrations, S-nidradine acts purely as a PAM; whereas, at higher concentrations, it acts as both a PAM and as an agonist in a manner reminiscent of other general anesthetics acting through this receptor (Fig. 3b, e; Supplementary Fig. 11b, i)[30]. Comparing nidradine with etomidate (Fig. 3b–d, Supplementary Fig. 11a–g), we found that S-nidradine has an approximately 3- to 4-fold lower PAM potency than etomidate (7 vs. 2 μM; Fig. 3b) yet it is similarly effective in enhancing the receptor's sensitivity to GABA (Fig. 3c). Indeed, we observed 3- to 5-fold potentiation in currents by nidradine in the presence of low GABA concentrations; however, at saturating GABA concentrations, S-nidradine does not further potentiate $GABA_A$ activity (Fig. 3d). The agonist potency of S-nidradine is ~10-fold weaker than that of etomidate (571 vs. 52.1 μM; Fig. 3e, Supplementary Fig. 11h and i). As concentrations that induce agonist activity are unlikely to be reached in vivo, we suggest that the anesthetic effect in zebrafish and mice occurs via S-nidradine's PAM activity.

To gain a detailed understanding of how S-nidradine binds to these receptors and to inform future structural optimization, we resolved a 2.9 Å structure of the α1β2γ2 receptor bound to S-nidradine via cryo-EM (Supplementary Fig. 12, Supplementary Table 5). We found that S-nidradine, like etomidate and propofol, binds to the β-α interfaces in the receptor's transmembrane domain (TMD, Fig. 4a). Although nidradine binds to both β-α TMD interfaces, one binding site has higher ligand occupancy. From our cryo-EM density map and model, S-nidradine is engaged in electrostatic interactions with N265 and T262 on the M2 helix of the β2 subunit via an amide oxygen and isoxazole nitrogen, respectively (Fig. 4b). Importantly, the key amino acids comprising the S-nidradine-binding site are conserved across humans, mice, and zebrafish, which is consistent with nidradine's cross-species activity and suggests strong potential for clinical utility (Fig. 4c). In any case, S-nidradine's binding site partially overlaps with those of propofol and etomidate. However, this compound binds deeply, towards the cytosol and slightly more inwards towards the pore than either propofol or etomidate (Fig. 4d). This binding mode allows S-nidradine to make hydrophobic interactions with residues located further down the receptor's subunit interface, beyond where etomidate and propofol reach (Supplementary Fig. 13a and b).

Since the strong electrostatic interactions between S-nidradine and the N265 and T262 residues were suggested by the cryo-EM data to be determinants of the compound's binding and activity, we substituted these amino acids via site-directed mutagenesis to test their importance. Specifically, we made N265I and T262V mutants and tested their function in electrophysiology experiments. To assess their influence on S-nidradine PAM activity, we co-applied GABA at EC5 (1 μM for WT, 0.5 μM for N265I, and 3 μM for T262V; Supplementary Fig. 13c–e) with S-nidradine at 7 μM, then at 100 μM, on cells expressing mutant and WT receptors. Both the N265I and T262V mutants showed a significant decrease in sensitivity to 7 μM S-nidradine versus the WT receptors. However, when GABA was co-applied with S-nidradine at the higher 100 μM concentration, only the N265I mutant showed a significant decrease in PAM activity (Fig. 4e, Supplementary Fig. 13f–h). To determine if these mutants also affected S-nidradine agonist activity, we applied S-nidradine alone at 300 μM and 1 mM on cells expressing WT and mutant receptors. Both mutants showed significant decreases in activity for both concentrations when compared to WT (Fig. 4e, Supplementary Fig. 13f–h). We conclude that both N265 and T262 are key determinants of S-nidradine PAM and agonist activity, and that both activities likely arise through occupancy of the same sites.

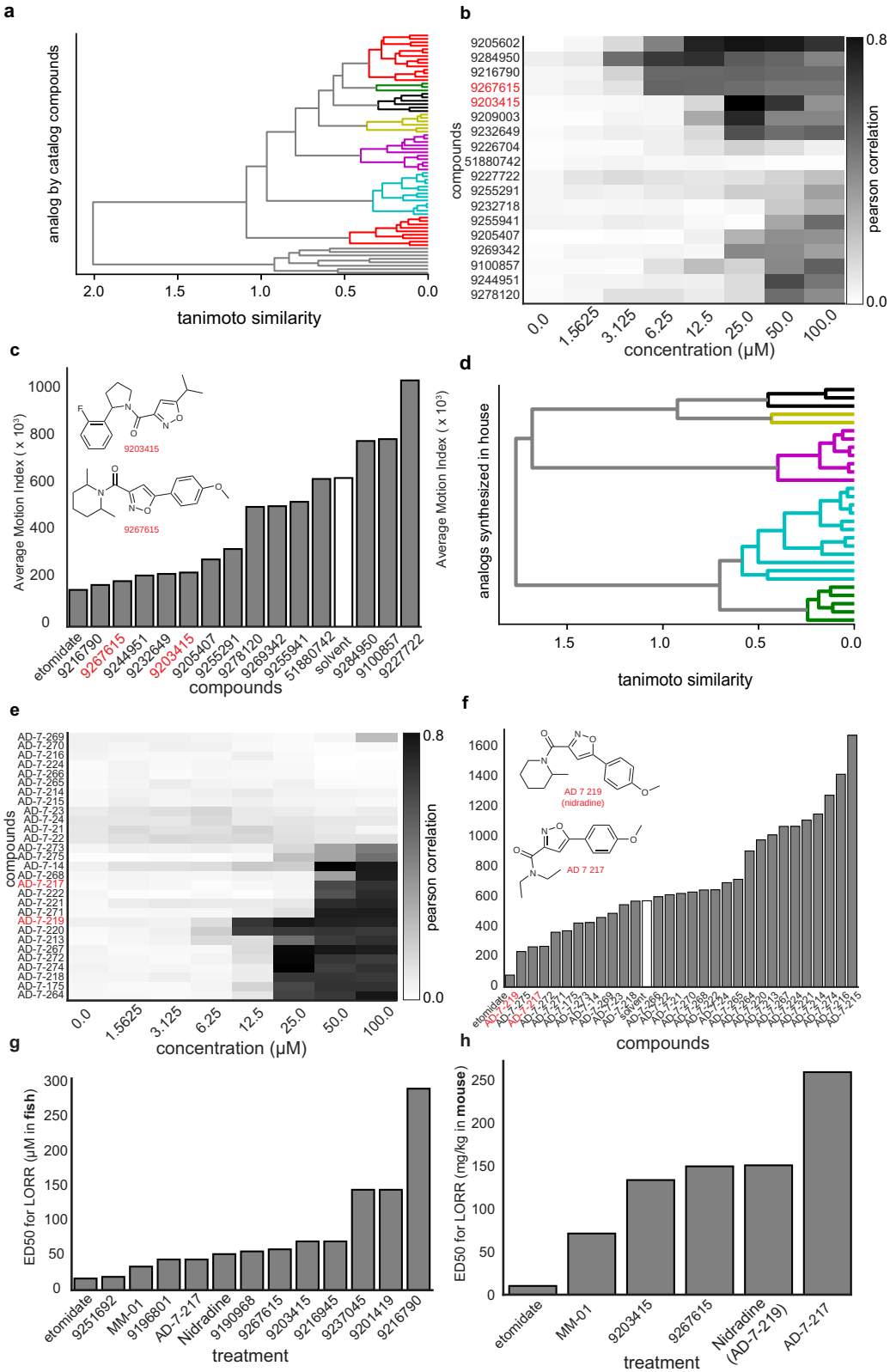
To test if S-nidradine exhibited PAM activity across other $GABA_A$ receptor subtypes, beyond the canonical synaptic α1β2γ2 subtype, we ran further co-application tests on the α4β2γ2, α5β2γ2, and α4β2δ subtypes, which are all found extrasynaptically[31,32] and share a conserved S-nidradine binding site (Supplementary Fig. 13i). These experiments showed that S-nidradine acts as a PAM at these subtypes and has similar or reduced PAM activity at lower concentrations when compared to the α1β2γ2 subtype (Supplementary Fig. 13j). Interestingly, the PAM activity of S-nidradine was significantly increased in the α5β2γ2 subtype compared to α1β2γ2 when it was co-applied at a higher (100 μM) concentration, indicating that the compound could be more efficacious at this subtype.

To gain a deeper understanding of how S-nidradine potentiates the α1β2γ2 receptor and how its mechanism compares to currently used general anesthetics, we next analyzed pore dimensions of the $GABA_A$ receptor bound to GABA alone, GABA + S-nidradine, GABA + etomidate, and GABA + propofol (Fig. 4f and g). While all of these structures are either in a desensitized or desen sitized-like state, the GABA + S-nidradine structure has the narrowest -2′ desensitization gate, with a diameter of 2.4 Å, compared to GABA + etomidate, GABA + propofol, and GABA-only pores having diameters of 2.9, 3.3, and 3.6 Å[4], respectively, at this same location. Interestingly, at the 9′ activation gate, the GABA + S-nidradine structure has a pore diameter of 5.7 Å, which is similar to the etomidate-bound structure's pore diameter of 6.2 Å. The GABA-only pore is smaller with a diameter of 4.6 Å, whereas the GABA + propofol structure's pore is much wider with a diameter of 10.4 Å. These findings indicate that S-nidradine's mechanism of potentiation may be similar to those of the currently used general anesthetics, where the compounds cause widening of the pore at the 9′ activation gate, likely destabilizing the resting state and sensitizing the channel to GABA potentiation[33].

Nidradine produces enhanced surgical anesthesia and analgesia

An important feature of many general anesthetics is their ability to generate surgical anesthesia, namely, loss of reflexive responses to noxious stimuli (i.e., nociceptive areflexia). For clinically relevant anesthetics (for example, volatile anesthetics[34], propofol[35,36], ketamine[37]), the doses that induce surgical anesthesia are generally higher than those that induce hypnotic effects. To systematically determine whether nidradine produces surgical anesthesia in mice, we assessed loss of reflexive withdrawal responses (LoWR) to 30 s of continuous strong pinch of the hindpaw. Interestingly, during our initial pilot testing of nidradine, we observed that mice lost withdrawal

https://doi.org/10.1038/s41467-026-79384-x



reflexes to noxious stimuli (hindpaw pinch) at the same dose that produces LoRR, which was unexpected. Therefore, we performed LoWR testing at approximately the ED_{50} for LoRR, for both nidradine and etomidate (Fig. 5a). As expected, at the ED_{50} dose for etomidate, mice that lost righting reflex continued to respond to strong hindpaw pinch (Fig. 5c). However, when the same test was conducted with nidradine, the withdrawal reflex to strong hindpaw pinch was absent in all mice that lost righting reflex (Fig. 5c). This phenomenon was also observed in adult zebrafish (Fig. 5b, Supplementary Movie 2). To the best of our knowledge, the equipotent production of hypnosis and surgical anesthesia (areflexia) is a distinguishing feature of nidradine.

https://doi.org/10.1038/s41467-026-79384-x

Fig. 2 | Analog development campaign of the primary oxazole lead (MM01). **a** Structural clustering of 70 commercially available "analog by catalog" compounds with >70% similar to MM01 (*y*-axis) yields 8 clusters using a Tanimoto similarity metric (*x*-axis). **b** Dose–response heatmap for 18 "analog by catalog" compounds (rows). Each cell shows the mean etomidate similarity phenoscore (color bar) across $n = 3$ wells at the indicated concentrations (columns); 0.0 denotes on-plate vehicle controls. **c** Validation of catalog analogs in adult zebrafish. Average motion index (MI) per compound; lower MI indicates reduced locomotor activity. Etomidate served as the positive control, vehicle as the negative control (solvent, white bar). Structures of the two strongest analogs are shown above the plot, with labels highlighted in red. **d** Structural clustering of 29 in-house–synthesized analogs, forming five clusters by Tanimoto similarity. **e** Dose–response heatmap for 29 in-house synthesized analogs (rows). Each cell shows the mean etomidate similarity phenoscore (color bar) across $n = 3$ wells, 8 fish/well at the indicated concentrations (columns); 0.0 denotes vehicle controls. **f** Validation of in-house analogs in adult zebrafish. Average MI per compound with labeled structures of the top two analogs (highlighted in red). Etomidate served as the positive control, vehicle as the negative control (solvent, white bar). **g** and **h** Bar plots showing ED_{50} of values (*y*-axis) in μM for zebrafish (**g**; $n = 6–8$) or mg/kg in mice (**h**; $n = 6–7$) for the parent molecule MM01, and the top analogs. Source data are provided as a Source Data file.

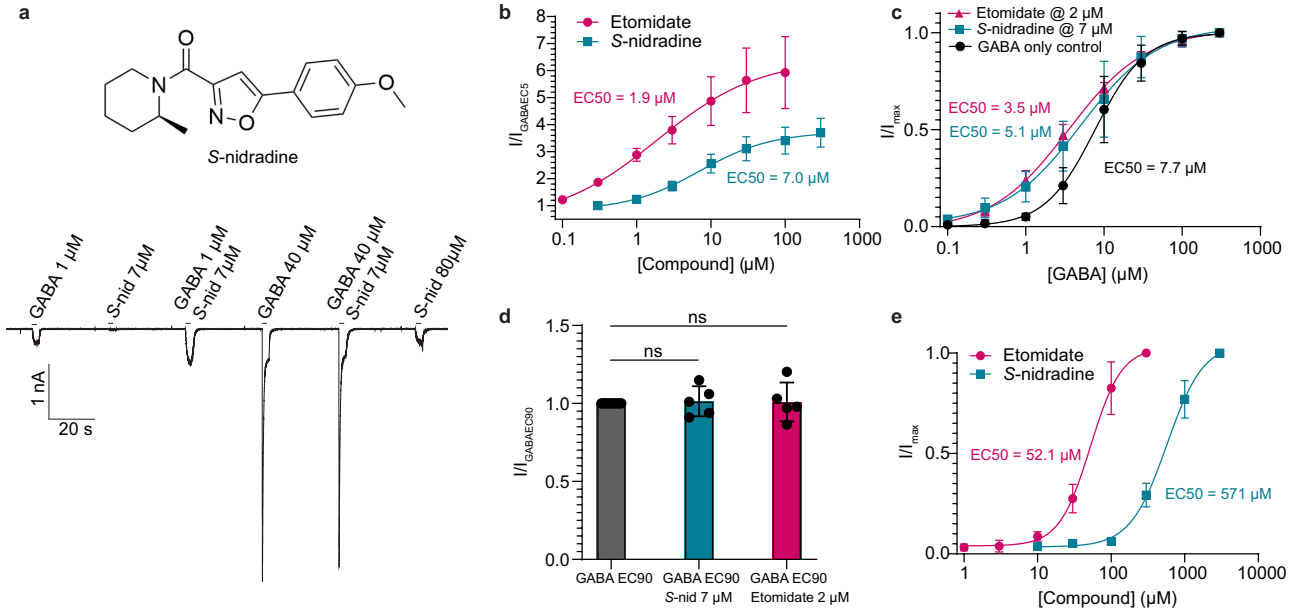


Fig. 3 | S-nidradine activity on the α1β2γ2 $GABA_A$ receptor. **a** Chemical structure of S-nidradine (upper) and whole-cell patch-clamp electrophysiology showing activity of S-nidradine on the GABAA receptor at different concentrations and in the absence and presence of GABA. **b** Electrophysiology showing dose-dependent effects of S-nidradine and R-etomidate (etomidate) on the receptor in the presence of GABA at EC5 (1 μM). Etomidate is more efficacious and more potent. $n = 5$ independent cells, error bars represent mean ± SEM. **c** Electrophysiology showing how fixed concentrations of S-nidradine and etomidate affect the dose-dependent activity of GABA. Both compounds enhance GABA activity, with the greatest effects occurring at low [GABA]. $n = 5$ (GABA only control and GABA + etomidate) and 6 (GABA + *S*-nidradine) independent cells, error bars represent mean ± SEM. **d** Effects of S-nidradine (S-nid) and etomidate on the receptor in the presence of high [GABA]; here, neither compound further increases GABAA receptor activity; $p = 0.7609$ for GABA alone vs. GABA + S-nid, p = 0.8691 for GABA alone vs. GABA + etomidate. $n = 5$ independent cells, error bars represent mean ± SEM. Two-tailed Welch's *t*-tests were used. **e** Both compounds are agonists on the receptor at concentrations well above the range where they are active as PAMs. $n = 4$ (etomidate) and 5 (*S*-nidradine) independent cells, error bars represent mean ± SEM. Source data are provided as a Source Data file.

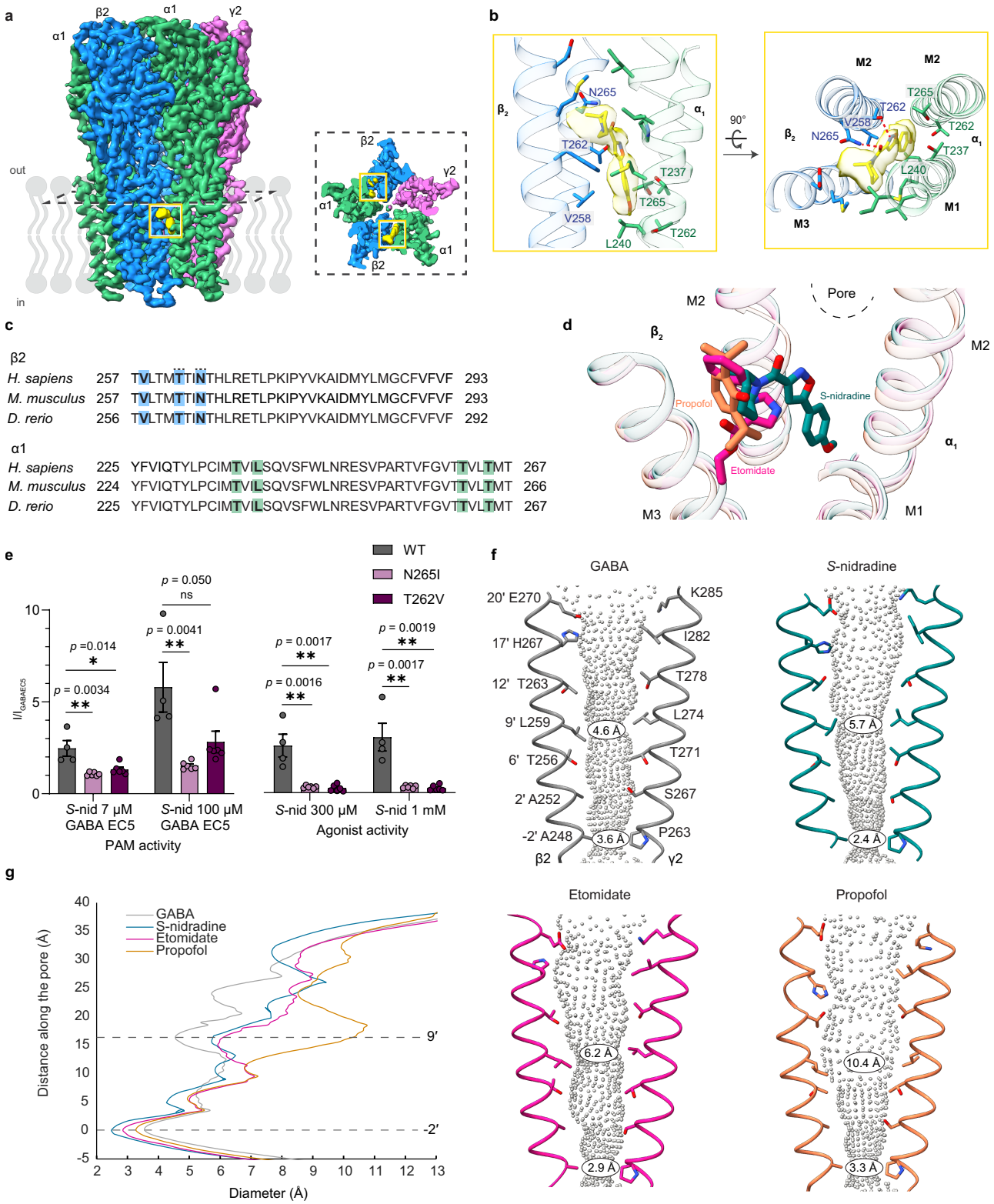
As nidradine produces surgical anesthesia (i.e., blocks withdrawal of the paw to a strong pinch) at lower than expected doses, we next asked whether nidradine also blocks nocifensive responses, a reflex correlate of pain processing, at subanesthetic doses. Importantly, our assessments were made at nonsedating doses (capable of staying on the rotarod) in awake mice (Supplementary Fig. 14a), such that any potential loss of responses to noxious stimuli would not erroneously be misclassified due to an inability of the mouse to respond. At that dose, we monitored nociceptive responses to a strong noxious heat stimulus produced by a short-duration, high-intensity infrared laser pulse in awake and freely moving mice[38]. As expected, subanesthetic doses of etomidate did not reduce nocifensive responses to the laser stimulus. In contrast, at subanesthetic doses, nidradine significantly reduced responses to the laser stimulus, compared to vehicle controls (Fig. 5d). Follow-up studies using light-induced acute noxious stimuli (i.e., optovin) confirmed that nidradine, but not etomidate, also reduces nocifensive responses in larval zebrafish (Fig. 5e) at subanesthetic concentrations (Supplementary Fig. 14b).

To better understand the mechanism underlying the anesthetic and analgesic actions of nidradine, we performed radioligand displacement profiling across a panel of neuroreceptors through the Psychoactive Drug Screening Program (PDSP)[39]. Nidradine did not bind α2 adrenergic receptors, which are targets of established anesthetics and analgesics (Supplementary Fig. 15), nor did it bind opioid receptors (mu, delta, kappa). Interestingly, nidradine did exhibit non-selective inhibition of voltage-gated sodium (NaV) channels (NaV1.4, NaV1.5, NaV1.6, NaV1.8); however, the low potencies (~140 μM) measured indicate that NaV channels are unlikely to contribute to the hypnotic or analgesic action of nidradine (Supplementary Fig. 16).

Discussion

In this drug development effort, we discovered a chemotype that not only produces general anesthesia but also analgesia at lower doses. This discovery was enabled by a highly informative behavioral phenotype in larval zebrafish induced by known general anesthetics. Our high-throughput compatible platform for behavioral profiling enabled target-agnostic screening of 12,000 molecules in larval zebrafish. Our lead molecule, developed from extensive hit-to-lead optimization efforts, nidradine, is a positive allosteric modulator of the $GABA_A$ receptor and shares binding sites with other clinically relevant

https://doi.org/10.1038/s41467-026-79384-x



general anesthetics. Nidradine is distinct from clinically used anesthetics in that it produces hypnosis and areflexia at the same dose.

A key observation in our study is that a secondary screen of anesthetic-like hits in adult fish after the primary larval zebrafish screen was an essential step toward translating anesthetic candidates to mammals. Because some compounds identified in larval zebrafish did not reproduce comparable anesthetic phenotypes in adult animals or mice, the secondary adult zebrafish screen served as an additional translational filter to prioritize compounds with activity across developmental stages and increase the likelihood of translation to mammalian systems. During development, zebrafish undergo maturation of GABAergic circuitry and synaptic connectivity, which can alter drug sensitivity and network-level responses[40–44]. Moreover, pharmacokinetic factors differ markedly between larvae and adults;

https://doi.org/10.1038/s41467-026-79384-x

Fig. 4 | Structural details of S-nidradine binding and mechanisms of potentiation. a Side view (left) and cross-section through the TMD (right) of the cryo-EM density map of the α1β2γ2 receptor with S-nidradine bound. α1 shown in green, β2 shown in blue, γ2 shown in purple, and S-nidradine in yellow. **b** Details of the S-nidradine binding site with some interacting residues shown. **c** Sequence alignment of the S-nidradine binding site, showing conservation across humans, mice, and zebrafish; residues important for S-nidradine binding are highlighted, and residues likely making electrostatic interactions with S-nidradine are labeled with a dotted line. **d** Superposition of the S-nidradine, etomidate, and propofol binding sites. **e** Electrophysiology comparing S-nidradine PAM and agonist activities on the WT, N265I, and T262V mutated receptors. GABA was co-applied at EC5 (1 μM for WT, 0.5 μM for N265I, and 3 μM for T262V) with S-nidradine at 7 μM, then at 100 μM. S-nidradine was then applied alone at 300 μM and 1 mM. $n = 4$ (WT) and 6 (N265I and T262V) independent cells, error bars represent mean ± SEM for all conditions; $^{*}p < 0.05$, $^{**}p < 0.01$, $^{***}p < 0.001$. Two-tailed Welch's *t*-tests were used. **f** HOLE representations of the α1β2γ2 GABAA receptor in the presence of GABA alone, GABA + S-nidradine, GABA + etomidate, and GABA + propofol (PDB IDs: 6X3Z, 9YNN, 6X3V, 6X3T). The diameters of the 9′ activation and -2′ desensitization gates are shown. **g** HOLE plot showing the diameter along the pore for the GABA only, GABA + S-nidradine, GABA + etomidate, and GABA + propofol structures. Source data are provided as a Source Data file.

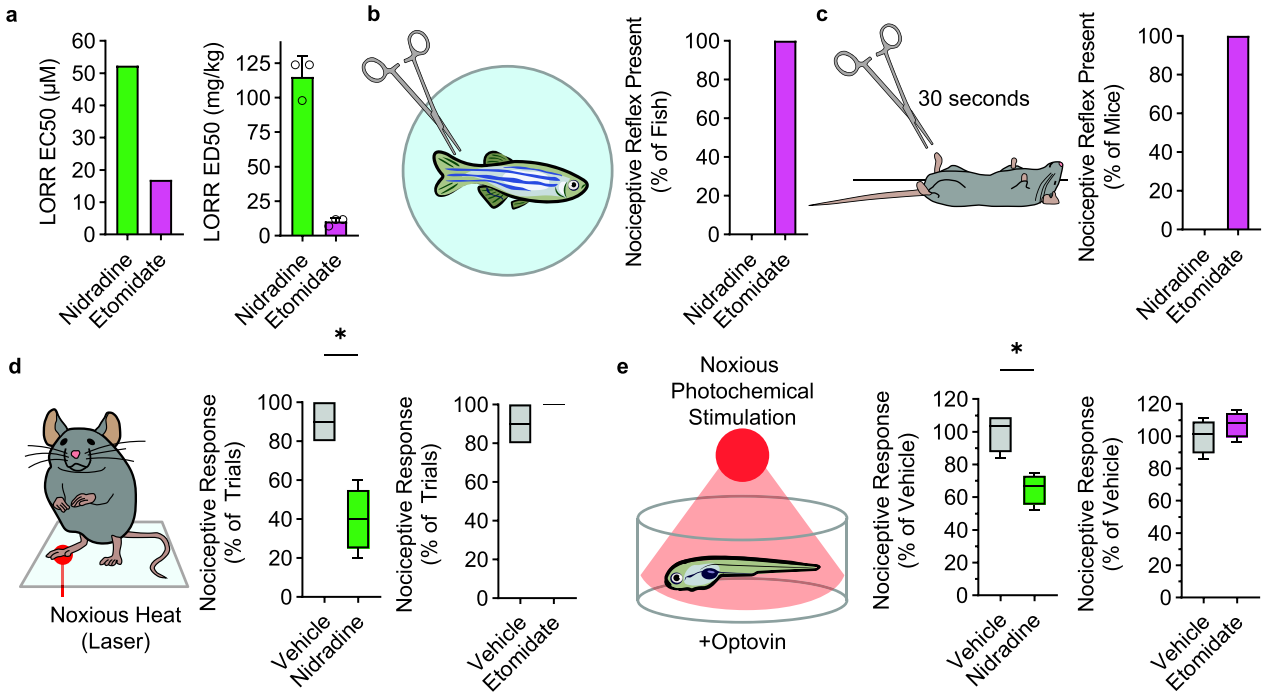


Fig. 5 | Nidradine produces surgical anesthesia and analgesia in fish and mice. a Dixon estimates of the loss of righting reflex (LORR) EC/ED_{50} in both adult zebrafish (μM, $n = 6$–7 fish) and mice (etomidate = 10.2 ± 1.6 mg/kg, $n = 6$–7 mice per Dixon estimate; nidradine = 115.1 ± 8.6 mg/kg; data indicate mean ± SEM). **b** In fish, withdrawal reflexes to noxious pinch are absent during administration of nidradine (25 μM) but are present during etomidate (3.125 μM) (nidradine: 0/5 fish responding; etomidate: 5/5 fish responding, $p \leq 0.0079$, Fisher's exact test). **c** In mice, withdrawal reflexes to noxious pinch are absent during administration of nidradine (115 mg/kg) but are present during etomidate exposure (12 mg/kg) (nidradine: 0/5 mice responding; etomidate: 6/6 mice responding, $p \leq 0.0022$, Fisher's exact test). **d** Sub-sedative doses of nidradine (27.5 mg/kg) reduce positive responses to noxious stimuli (5 trials each mouse) in mice (vehicle: median =90%, 25 Percentile = 80%, 75th percentile = 100%, $n = 4$ mice; nidradine: median = 40%, 25th percentile = 25%, 75th percentile = 55%, $n = 4$ mice; $p = 0.0286$, two-tailed Mann–Whitney test) but etomidate does not (vehicle: median = 90%, 25th percentile = 80%, 75th percentile = 100%, $n = 4$ mice; etomidate: median = 100%, 25th percentile = 100%, 75th percentile = 100%, $n = 4$ mice; $p = 0.4286$, two-tailed Mann–Whitney test). **e** Sub-sedative doses of nidradine (3.125 μM) reduce positive responses to noxious stimuli in fish (nociceptive responses are normalized to the vehicle control (optovin + vehicle), which was set to 100%; vehicle: median = 103.5%; 25th percentile = 87.5%; 75th percentile = 108.9%, $n = 4$ wells with 8 fish per well; nidradine: median = 66.8%, 25th Percentile = 55.5%, 75th percentile = 73.0, $n = 4$ wells with 8 fish per well; $p = 0.0286$, two-tailed Mann–Whitney test), but etomidate (469 nM) does not (normalized to vehicle control; vehicle: median = 101.5%, 25th percentile = 89.4%, 75 Percentile = 109.1%, $n = 4$ wells with 8 fish per well; etomidate: median = 108.1%, 25th percentile = 99.3%, 75th percentile = 114.4%, $n = 4$ wells with 8 fish per well; $p = 0.4857$, two-tailed Mann–Whitney test). In panel **a**, bars indicate the mean, and error bars indicate SEM. In panels **d** and **e**, in the box and whisker plots, the center line indicates the median, lower and upper bounds of the box indicate the 25th and 75th percentile, respectively, and whiskers indicate the 5th and 95th percentile. Source data are provided as a Source Data file. Original adult and larval zebrafish illustrations were created by Kaity Hammerstein; original mouse illustrations were created by coauthor Jarret A.P. Weinrich.

larval fish are small, with limited diffusion barriers and have a rudimentary blood–brain barrier that may allow easier compound penetration[24,45,46]. For this reason, confirming that candidate compounds produce anesthesia in adult fish, particularly compounds that induce rapid LoRR within minutes, is key to identifying compounds with appropriate kinetics, bioavailability, and pharmacodynamics for translation into mammals.

The chemotypes discovered in the screen are structurally distinct from all known general anesthetics- the ethers (sevoflurane), alkyl phenols (propofol), cyclohexanones (ketamine), imidazoles (etomidate and dexmedetomidine), and the benzodiazepine remimazolam. Though our primary hit MM01 contained an oxazole, iterative SAR optimization led to the identification of a related isoxazole scaffold. The isoxazole ring is a well-recognized CNS-privileged heteroaromatic moiety that is amenable to medicinal chemistry, appearing in multiple

synthetic and naturally occurring neuroactive compounds, including the GABAergic agonist muscimol from Amanita mushrooms[47]. Recent systematic analyses of isoxazole derivatives further highlight this chemotype's broad bioactivity across CNS, anti-inflammatory, antimicrobial, and anticancer indications, underscoring its suitability as a privileged scaffold for the development of anesthetics and many other therapeutics[23,47–51].

All anesthetics that produce surgical anesthesia (loss of responses to noxious stimuli) do so at doses greater than those that induce hypnosis (i.e., loss of consciousness)[52]. For example, for volatile anesthetics, the concentration of anesthetic that produces loss of volitional responses is generally 30–50% of the dose required for loss of response to surgical incision[52,53]. Similarly, intravenous general anesthetics, such as propofol[54–56] and etomidate[57], also block reflexes to noxious stimuli at doses above those that induce hypnosis. In distinct contrast, nidradine blocks noxious stimulus-evoked reflexes at the lowest doses that block the righting reflex. This enhanced surgical anesthetic effect, coupled with analgesia at subsedative doses, could prove useful for clinical scenarios where lighter levels of anesthesia are typically sufficient, such as procedures in the emergency department or prehospital trauma care[58,59]. Currently, we do not know the mechanism through which nidradine blocks nociceptive reflexes in the setting of surgical anesthesia. Interestingly, targeted mutations to the β2 and β3 subunits of the $GABA_A$ receptor (N265), which is a part of a shared binding site in the $GABA_A$ receptor targeted by etomidate, propofol, and nidradine, reduces[60], or even abolishes[61], the generation of surgical anesthesia by etomidate and propofol. This possible receptor interaction suggests that nidradine's equipotent production of surgical anesthesia and hypnosis may be due to differential interactions with the $GABA_A$ receptor, one possibility being increased selectivity at specific subunit combinations that may enhance inhibitory effects on spinal motor or reflex circuits[62–64]. It is also possible that nidradine's antinociceptive effects occur through an undetermined receptor; however, we have ruled out voltage-gated sodium channels, α2 adrenergic receptors, and opioid receptors. Additionally, while NMDA receptor antagonists can produce anesthesia (ketamine, nitrous oxide), this class does not reliably produce surgical anesthesia in mice[34,65], so it is unlikely that NMDA receptor antagonism can account for the enhanced surgical anesthesia that is produced by nidradine.

The ability of nidradine to produce analgesia at subsedative doses places it in a small class of anesthetics that can provide pain relief in awake animals. As others have shown, and we have confirmed with etomidate, most general anesthetics that act at the $GABA_A$ receptor are not analgesic at subsedative doses (e.g., propofol[10], isoflurane[66], and sevoflurane[67]). It is unlikely, therefore, that the analgesic effects of nidradine in awake animals are derived from $GABA_A$ receptor PAM activity. Subsedative doses of NMDA receptor antagonists, such as anesthetics like nitrous oxide[38] and ketamine[68], produce at best a minimal effect on the production of reflexes to noxious stimuli in mice, which suggests that nidradine acts through a separate mechanism from these compounds to produce analgesia. While psychedelics have shown promise in treating chronic pain[69], recently published work indicates psychedelics do not alter the production of reflexive pain behaviors in naïve mice[70]. Furthermore, nidradine does not bind the 5-HT2A receptor, further ruling out this receptor mechanism for analgesia. Recently published work has identified that the anti-anhedonic effects of propofol are mediated through direct binding of propofol to the dopamine transporter (DAT)[71]; however, DAT and the dopamine receptors (D1-5) are also not targets of nidradine. In future studies, we will investigate the molecular mechanism under nidradine's production of analgesia. Importantly, by recapitulating the analgesic effects of nidradine in larval zebrafish, we will incorporate the ability to identify analgesic general anesthetics into our high-throughput discovery pipeline.

Methods

Ethics statement

All research was performed in accordance with relevant ethical regulations. All zebrafish and mouse experiments were conducted in accordance with protocols approved by the Institutional Animal Care and Use Committee (IACUC) at the University of California, San Francisco (UCSF; protocol AN201827 for zebrafish and protocol AN203168 for mice). Human adrenal cortex tissue was obtained through a UCSF institutional core service that facilitates the collection of cadaveric donor tissue under an Institutional Review Board (IRB)-authorized tissue procurement protocol for the recovery of viable human organs, including intact adrenal glands (UCSF IRB Study No. 20-31618; reference No. 299595).

Fish maintenance, breeding and chemical treatments

Wild-type zebrafish (Singapore strain) were maintained and bred according to standard zebrafish husbandry procedures[72] and staged in days post-fertilization (dpf). All embryos were raised on a 14/10-h light/dark cycle at 28 °C until 7 dpf. Young embryos and larvae were maintained in egg water prepared from Instant Ocean sea salts. Stock salts were prepared by dissolving 40 g Instant Ocean Sea Salts in 1 L distilled water. Egg water was prepared by diluting 1.5 mL stock salts into 1 L distilled water, and the pH was adjusted to 7.0 using sodium bicarbonate. Larvae were anesthetized with ice-cold egg water and distributed 8 animals per well into square 96-well plates (GE Healthcare Life Sciences) with 300 μL of egg water[72]. Sex was not considered a biological variable in larval experiments because zebrafish have not yet undergone sex differentiation at the developmental stages examined. For anesthesia assessments, adult AbTL or TuAB fish were placed individually in the well of a round six-well plate in 8 mL of egg water. Chemicals were applied directly to the egg water, and larvae were incubated at room temperature for 1 h before behavioral analysis. Adult animals were assayed immediately following drug treatment. For secondary screening of hit compounds in adult zebrafish loss of righting reflex assays, single-animal experiments were performed at 50 μM. For Dixon ED_{50} estimates, each compound was tested with $n = 5$ animals. Adult zebrafish were selected at random from mixed-sex populations; the sex of individual animals was not recorded, and the experiments were not designed to assess sex-dependent differences.

Chemical libraries

All chemical libraries were dissolved in DMSO. The Chembridge library (Chembridge Corporation) contains 12,000 compounds at 10 mM, a commercially available diversity-oriented small-molecule collection designed to provide broad scaffold and pharmacophore coverage across drug-like chemical space. Compounds in the library were selected for favorable medicinal chemistry properties, including structural diversity and synthetic tractability. The complete list of compounds screened, including their InChIKeys, is provided in Supplementary Data File 1. All compounds were diluted in egg water and screened at 30 μM final concentration in <1% DMSO. Controls were treated with an equal volume of DMSO. All previously annotated and hit compounds were validated in 3–12 replicate well plates in a dose response behavioral assay, 8 zebrafish larvae per well at concentrations ranging from 100 to 1.56 μM.

Automated behavioral phenotyping assays

Plates were illuminated with a 850 nm infrared light from a custom-built led array. Digital video was captured at 25 frames per second using an AVT Pike digital camera (Allied Vision). Assays' duration was 30–120 s, consisting of a combination of acoustic and light stimuli. Low (60 db) and high (70 db) amplitude acoustic stimuli were delivered using push-style solenoids (12 V) to tap a custom-built stage where the 96-well plate was placed. Light stimulus was delivered using

high-intensity LEDs (LEDENGIN) that delivered violet (405 nm, 11 μW/mm^2), blue (460 nm, 18 μW/mm^2), green (525 nm, 11 μW/mm^2), and red (650 nm, 11 μW/mm^2) wavelengths. Stimuli and digital recordings were applied to the entire 96-well plate simultaneously. Instrument control and data acquisition were performed using custom Python scripts. The zebrafish motion index (MI) was calculated as follows:

$$MI = \Sigma\,|frame_n - frame_{n-1}| \quad (1)$$

Normalized MI (nMI) was calculated as follows:

$$nMI = [MI - min(MI)]/[max(MI) - min(MI)] \quad (2)$$

For motion estimation expressed as a CD(10), the value was estimated as the count of pixels that changed from the previous frame by intensity ≥ 10/255. Detailed descriptions of the behavioral assays are described here[17,73–75].

Zebrafish nocifensive response assays

Zebrafish nocifensive responses were assessed using optovin (Tocris) at a final concentration of 1.5 μM in the presence or absence of nidradine at a sub-sedating concentration (1.56 μM). Optovin was activated using a 5 s pulse of violet light, and motor responses were quantified following stimulation. Behavioral responses were averaged across 5 light pulses separated by 1 min interstimulus intervals. Adult zebrafish areflexia was assessed in randomly selected animals from mixed-sex populations using a tail-pinch stimulus applied for <1 s, and behavioral escape responses were scored. Individual animal sex was not recorded.

Mouse husbandry

All mouse husbandry and surgical procedures adhered to the regulatory standards of the Institutional Animal Care and Use Committee of the University of California, San Francisco (UCSF; protocol AN203168). Mice were kept on a 12-h light/dark cycle with access to food and water ad libitum. The environment is kept to 18–23 °C and 40%–60% humidity.

Pharmacokinetic Studies in Mice

Pharmacokinetic studies were performed in male C57BL/6 mice (8–12 weeks old, 25 ± 5 g) following a single intraperitoneal administration of nidradine at 30 mg/kg (10 mL/kg dosing volume; formulation concentration 3 mg/mL). Animals were sampled using a sparse sampling design (n = 3 animals per time point; total n = 24). Plasma, cerebrospinal fluid (CSF), and brain samples were collected at 0.25, 0.5, 1, 2, 4, 6, 8, and 24 h post-dose. Blood samples were collected into K2EDTA-containing tubes and centrifuged at approximately 11,000×g for 10 min at 4 °C to isolate plasma. CSF samples were collected under isoflurane anesthesia, and brains were harvested following PBS perfusion under deep isoflurane anesthesia. Samples were stored at −70 °C prior to analysis. Plasma, CSF, and brain homogenate concentrations of nidradine were quantified using a fit-for-purpose LC–MS/MS bioanalytical method. Pharmacokinetic parameters were calculated using non-compartmental analysis in Phoenix WinNonlin (version 8.3 or higher), with AUC values determined using the linear trapezoidal method. Nidradine was formulated in Kolliphore EL:EtOH (7:1) and diluted into saline immediately before administration.

Mouse behavioral assays

Compound solubilization for mouse behavior testing. Prior to testing, compounds were solubilized in 1.5% ethanol, 11% kolliphor EL (Sigma-Aldrich, C5135-500G), and 87.5% sterile saline. Dry compounds were first mixed with a solution of ethanol and kolliphor, then diluted with saline immediately prior to testing. Maximum intraperitoneal injection (IP) volume was set to 0.5 cc.

LoRR testing. To assess the hypnotic effects of known and candidate general anesthetics, we assayed mice for the presence of loss of righting reflex (LoRR) after compound administration. Mice were tested in a behavioral arena that consisted of a four-walled, 12″ by 12″ acrylic chamber. The chamber was placed onto a heating pad whose temperature is maintained by circulating warm water (40 °C). To initiate the testing session, compounds were administered via IP injection, after which mice were carefully placed into the behavioral arena and closely monitored for 10 min post-injection. Mice were assayed for LoRR approximately every 30 s. During assessment for LoRR, the tester attempted to gently place the mice into the supine position. A positive LoRR response was scored as the continuous, unaided maintenance of the supine position for 30 s. After the 10-min testing session, mice were monitored for the recovery of righting reflex (RoRR). Positive RoRR was defined as 3 consecutive failed LoRR tests after the mice first reestablished the prone position (all 4 paws on the chamber floor), test performed every 30 seconds.

LoWR testing. To assess for nociceptive areflexia, we assayed mice for the presence of loss of withdrawal reflexes (LoWR) after compound administration. First, mice were injected (IP) with the compound, then assessed for LoRR within 10 min after injection within the same arena described above. After LoRR was achieved, LoWR testing was initiated. The LoWR test consisted of pinching the mouse's hind paw with an extra-long hemostat (23 cm), without engaging the locking mechanism. Positive LoWR was defined as a lack of observable reflexive hindlimb withdrawal response to 30 s of continuous pinch.

Pain testing. To assess for analgesic effects of subsedative doses of general anesthetics, we assessed for changes to pain responses following acute noxious thermal stimuli delivered by high-intensity, short-duration infrared laser pulse, using a protocol adapted from our previous study[38]. The laser stimulus was generated by a LASMED (Lass-7M) 7 W 975 nm laser set to a laser power of 1750 mA and pulse duration of 300 ms. Briefly, mice were placed within a chamber with a glass floor that allows for the presentation of the noxious laser stimulus to the plantar surface of the hind paw. During a testing session, the laser stimulus is presented to one of the two hindpaws 5 times, with a cooldown period of at least 3 min between individual trials. The left and right hindpaws were stimulated in an alternating fashion. Positive nociceptive responses to laser stimuli were considered as the withdrawal of the hindpaw from the glass floor, shaking of the hindpaw or hindlimb, and licking of the hindpaw. Laser testing sessions began 30 min after the injection (IP) of either vehicle, etomidate, or nidradine. Prior to the testing day, mice were habituated to the testing chamber for at least 30 min.

Rotarod testing. To establish the sedative doses of known and candidate general anesthetics, we performed rotarod testing[76]. Here, mice were placed onto an accelerating spinning rod, and the time to fall from the rod was recorded. Mice were considered sedated if they fell off the rotarod within 120 s of testing. Mice were tested 30 min after compound injection (IP). Prior to testing, mice were trained to perform the rotarod test, and mice were considered trained only after they could remain on the rotarod without falling for at least 5 min.

Estimation of ED_{50} values using Dixon's Up/Down method. To estimate the effective dose that produces a desired effect (i.e., LoRR) during 50% of testing sessions (ED_{50}), we used Dixon's Up/Down method[27]. To perform the Dixon method, an initial test was performed at the desired starting dose. If the test was positive for the effect (i.e., LoRR occurs), the dose was halved for the subsequent test. If the test was negative (i.e., no LoRR), then the dose was doubled. This testing paradigm continued until the first change in response direction (i.e., in a series of positive tests, the first negative test, or vice versa), and then

4 more tests were performed after this change in direction. After this, the response observations (X for a positive response, O for a negative), the dosing scale (d, equal to 2), and the concentration of drug on the final test (x_{final}), are recorded. The response observations were compared to a lookup table generated in the original Dixon paper to generate the k-value. Then, to generate an estimate of the ED_{50}, the x_{final}, d, and k values are applied to the Dixon equation:

$$\log_2(ED_{50}) = x_{final} + dk \quad (3)$$

Voltage-gated sodium channel profiling

Cell culture. Human Embryonic Kidney (HEK) 293 cells stably expressing human NaV1.4/β1, NaV1.5/β1 and NaV1.6/ β1 (SB Drug Discovery, Glasgow, UK) and Chinese Hamster Ovary (CHO) cells stably expressing human NaV1.8/β3 in a tetracycline-inducible system (ChanTest, Cleveland, OH, USA) were cultured in Minimum Essential Media Eagle (MEM) with 10% fetal bovine serum (FBS), 2 mM L-glutamine and selection antibiotics as per manufacturer's recommendations. Cells were grown in a 5% CO_2 incubator at 37 °C and passaged every 3–4 days at 70–80% confluency using TrypLE Express (Invitrogen). hNav1.8 expression was induced by addition of tetracycline (1 µg/mL) and incubation at 28 °C for 48 h prior to assays.

Electrophysiology

Automated whole-cell patch-clamp recordings were performed with a QPatch II automated electrophysiology platform (Sophion Bioscience, Ballerup, Denmark) using single-hole (QPlate 16 with a standard resistance of 2 ± 0.4 MΩ) or multi-hole (QPlate 16X with a standard resistance 0.2 ± 0.04 MΩ, NaV1.8 only). Whole-cell currents were filtered at 8 kHz and acquired at 25 kHz and the linear leak was corrected by P/4 subtraction (leak potential −90 mV, leak sweep amplitude 10%). Series resistance across recorded cells ranged between 5 and 10 MΩ.

The extracellular solution (ECS) consisted of (in mM) 145 NaCl, 4 KCl, 2 $CaCl_2$, 1 $MgCl_2$, 10 HEPES, and 10 glucose, pH 7.4 with NaOH (adjusted to 305 mOsm/L with sucrose). The intracellular solution (ICS) consisted of (in mM) 140 CsF, 1 EGTA, 5 CsOH, 10 HEPES, and 10 NaCl, pH 7.3 with CsOH (adjusted to 320 mOsm/L with sucrose). TTX (1 µM) was added to the ECS for NaV1.8 recordings to inhibit background endogenous TTX-sensitive current in CHO cells.

Cumulative concentration–response curves were obtained at a holding potential of −90 mV using 50 ms depolarizing pulses to −20 mV (or +10 mV for NaV1.8) delivered every 20 s (0.05 Hz). A 1:1 mixture of Nidradine (R)- and (S)-enantiomers, prepared from 100 mM DMSO stocks, was diluted in ECS containing 0.1% Pluronic F-127 and applied to cells for 2 min at the indicated concentrations. Peak currents were normalized to the buffer control and fitted with a four-parameter Hill equation with a variable Hill coefficient.

In vitro mammalian receptor profiling

In vitro binding assays and Ki data were generated by the National Institute of Mental Health's Psychoactive Drug Screening Program (PDSP), contract no. HHSN-271-2008-00025-C (NIMH PDSP), for assay details: https://pdsp.unc.edu/pdspweb/content/UNC-CH%20Protocol%20Book.pdf[39].

Identification of phenotypically related compounds

To compare multi-dimensional behavioral profiles from the large-scale screen, we first defined a reference profile against which all other wells were evaluated. The prototypical profile for etomidate was generated by averaging six replicate wells treated with 6.25 µM etomidate. Phenoscore distances were then computed between each test well and this reference profile using the Pearson correlation distance (implemented in SciPy 1.11.4, Python 3.11.4). The phenoscore ranges from −1 to +1, with positive and negative values indicating positive or negative correlation, respectively; negative scores reflect anti-correlation. In practice, phenoscores saturated at ~0.7, which indicates a strong positive correlation given that the MI time series comprises vectors with 19,000 values. Ranking the screening hits: phenoscores were computed to assign each compound in the screening library a rank order and visualized using Supplementary Data File 2. Hit compounds were defined as the top 69 scoring compounds from this ranked list.

Cortisol detection assay

Isolation and detection of whole-larval cortisol were performed using a method adapted from Yeh et al. [77]. Thirty larvae were used per condition and treated with their respective compounds for 1 h. Animals were then anesthetized in ice-cold egg water after excess water was removed from samples, and were frozen in an ethanol/dry ice bath. Animals were then homogenized in 100 µL of H_2O, 1 mL of ethyl acetate was added to dissolve cortisol from the sample, the supernatant was collected and vaporized. Cortisol was dissolved in 0.2% Bovine serum albumin (A7030, Sigma) and frozen. For cortisol ELISA experiments, the commercially available colorimetric competitive enzyme immunoassay kit (Enzo-ADI-900-071) was used as instructed. Reaction was stopped using 1 M H_2SO_4. Absorbance was read at 450 nm in an ELISA plate reader (Biotek H4).

Ex vivo human adrenal gland cortisol detection assay

Donor organ collection. Normal human adrenal glands from a cadaveric donor were obtained through a core facility service (UCSF VITAL) maintained by our institution's solid organ transplant program[78]. The UCSF institutional core service facilitates the collection of cadaveric donor tissue under an IRB-authorized tissue procurement protocol for the recovery of viable human organs, including intact adrenal glands (UCSF IRB Study Number 20-31618, reference number 299595). The donor tissue was provided in de-identified and completely anonymized form. The research team did not have access to any identifiable donor information or medical records. Ethical oversight and stewardship of the cadaveric donor tissue procurement process was governed by a robust regulatory framework based on a non-living human participants research designation by the UCSF IRB.

Bilateral adrenal glands were recovered from suprarenal fat that had been dissected from donor kidneys being prepared for transplant. The interval between donor cross-clamp time and initiation of the experiment in the laboratory was approximately 12 h. After arrival at the laboratory, adrenal gland identity was confirmed morphologically and by observation of intrinsic adrenal gland autofluorescence under near-infrared (NIR) illumination using a Fluo-Optics Fluobeam device. All tissue processing procedures in the laboratory were performed on ice. The right and left adrenal glands weighed 4.2 and 5.0 g, respectively. Both glands were sectioned into ~1-mm-thick slices, and individual slices were trimmed into 40 mg tissue aliquots for experimental use.

Each tissue piece was immediately transferred into the upper chamber of a 24-well Transwell insert (polycarbonate membrane, 0.4 µm pore size, Corning) containing culture medium, while the lower chamber was filled with 600 µL of the same medium. Tissues were maintained on ice until the initiation of the ex vivo cortisol secretion assay.

To verify tissue viability, several randomly selected tissue slices were stained with Hoechst 33342 and propidium iodide (PI) according to our laboratory's standard protocol[79] (Supplementary Fig. 9).

Ex vivo cortisol secretion assay. A total of 18 independent adrenal tissue pieces (40 mg each; 9 specimens from the right adrenal gland and 9 specimens from the left adrenal gland) were used for cortisol secretion experiments. Before treatment, the Transwell inserts were equilibrated for 30 min at 37 °C in a humidified 5% CO_2 incubator with fresh culture medium replaced in the lower chambers every 15 min.

Following equilibration, tissue was transferred into fresh wells containing 600 µL of DMEM/F12 (1:1) medium (HyClone™ Classical Liquid Media, Cytiva; SH30261.01) supplemented with L-glutamine, HEPES, and sodium pyruvate for the determination of baseline cortisol secretion during a 30-min incubation.

After baseline collection, each insert was sequentially transferred to fresh wells containing one of three treatment conditions: ACTH + vehicle (DMSO), ACTH + nidradine, or ACTH + etomidate. Human ACTH (1–24) (ANASPEC, AS-20613) was used at a final concentration of 1 nM. Nidradine and etomidate were dissolved in DMSO to prepare 60 mM stock solutions immediately before the experiment and diluted into culture medium to a final concentration of 10 µM. Vehicle-treated samples received the corresponding volume of DMSO. Each treatment group consisted of six independent tissue samples, including three tissue pieces from each adrenal gland.

Transwell inserts were transferred to fresh treatment medium every 30 min, with simultaneous replacement of the medium in the upper chamber. Medium from the lower chamber was collected at 30-min intervals throughout the experiment. Cortisol concentrations were measured in samples collected after the baseline incubation and after 60 and 120 min of treatment. At each collection time point, 350 µL of medium from the lower chamber was harvested and stored at −80 °C until cortisol analysis.

Cortisol concentrations were determined using a commercial ELISA kit (MP Biomedicals Cortisol ELISA Kit, MP07M21603) according to the manufacturer's instructions. All samples were analyzed in duplicate. Absorbance was measured at 450 and 620 nm using an Absorbance 96 microplate reader (Byonoy, Germany). Cortisol secretion from each tissue piece was normalized either to its own baseline value and expressed as a percentage of baseline or to the wet weight of the adrenal tissue. Data from all groups were normally distributed, as assessed by the Shapiro–Wilk normality test. Statistical analyses were performed using one-way ANOVA followed by Tukey's post hoc multiple-comparisons test in GraphPad Prism (GraphPad Software, LLC).

Telemetric probes implantation

Blood pressure (BP), heart rate (HR), and body temperature (BT) were measured using a telemetric probe device (HD-X10; Data Science International). Briefly, under anesthesia and aseptic conditions, the probe device was placed in the mouse abdomen, and a subcutaneous tunnel was created from the neck to the abdominal skin, through which a catheter (connected to the probe) was pulled and then inserted into the left carotid artery. After the catheter was ligated using a 7-0 silk suture, the abdomen and incision on the neck were closed with a 6-0 absorbable Vicryl suture in a continuous pattern, and the skin layer was closed with a 6-0 silk suture in a continuous pattern. The mice were returned to the home cage and recovered on a warming pad.

Three weeks after the implantation of the telemetric probes, the implanted mice were singly housed in a cage that was placed on top of the DSI receiver (for probe signal detection). We monitored the BP, HR, and BT continuously over 2 h, in the following manner: 15 min (for baseline) and then for 105 min after injection of the compound. Data was acquired using the Ponemah Telemetry acquisition software (DSI), and percent changes were presented relative to each mouse's baseline. Recordings occurred every week, with a different compound. The implanted mice were euthanized at the end of all the tests.

Structural clustering

Structural clustering was performed using custom-written Python scripts. The RDKit Morgan fingerprint function was used to convert molecular structures into a digital hash. The SciPy hierarchical clustering (fcluster, linkage) and distance (pdist, parameters: metric = 'jaccard') functions were used to cluster the resulting molecular fingerprints.

α1β2γ2 $GABA_A$ receptor expression and purification

A tri-cistronic construct was used to express the α1β2γ2 $GABA_AR$ as described previously[4]. In brief, the three genes coding for each subunit were cloned into the pSBtet expression vector in the following order: β2-γ2-α1. For cryo-EM experiments, the intracellular loop between M3 and M4 for all subunits was replaced with a 7-amino acid linker, SQPARAA[80,81]. This EM construct also contains a strep tag on the γ2 subunit. Stable cell lines were created via a Sleeping Beauty transposon system[82,83]. Adherent HEK293S GnTI$^-$ cells were co-transfected with 1.9 µg of the pSBtet vector (pSBtet-GP, item #60495) carrying the EM construct as well as 0.1 µg of the transposase carrying vector, SB100X (pCMV(CAT)T7-SB100, item #34879). Lipofectamine2000 (Invitrogen) was used for transfection following the manufacturer's protocol. 24 h after transfection, selection of cells was initiated by incubation with 1 µg/mL puromycin. Selection was monitored by cell fluorescence and was terminated when all cells showed fluorescence. The adherent HEK293 GNTI$^-$ cells were then moved into suspension and expanded to a total of 6.4 L. When they reached a density of 3.5–4 × 10^6 cells/mL, protein expression was induced with 2 µg/mL doxycycline, and the cells were incubated with shaking at 30 °C with 8% CO_2.

Cells expressing $GABA_ARs$ were harvested through centrifugation and resuspended in 20 mM Tris, pH 7.4, 150 mM NaCl (TBS buffer) containing 1 mM phenylmethanesulfonyl fluoride (PMSF; Sigma-Aldrich) and 2 mM GABA (Sigma-Aldrich) before lysing with an Avestin Emulsiflex. The lysed cells were then centrifuged at ~7200×*g* for 15 min at 4 °C. The resulting membrane-containing supernatant was then centrifuged at ~18,000×*g* for 2 h at 4 °C. The membrane pellets were then homogenized using a Dounce homogenizer and solubilized in TBS buffer enriched with 40 mM n-dodecyl-β-D-maltoside (DDM, Anatrace), 1 mM PMSF, and 2 mM GABA for 1 h at 4 °C with nutation. Solubilized membranes were then centrifuged at ~18,000×*g* for 40 min at 4 °C. The supernatant was passed through Strep-Tactin XT Superflow affinity resin (IBA-GmbH). The resin was washed previously with TBS buffer containing 2 mM DDM, 0.01% (w/v) porcine brain polar lipids (Avanti), and 2 mM GABA. Protein was eluted with TBS buffer supplemented with 2 mM DDM, 0.01% (w/v) porcine brain polar lipids, 2 mM GABA, and 50 mM biotin (Sigma-Aldrich).

Nanodisc reconstitution

The plasmid used for saposin A expression was kindly provided by Salipro Biotech AB. Nanodisc reconstitution followed the same protocol as described previously[4,84]. Concentrated receptors were first mixed with porcine brain polar lipids before incubation at room temperature for 10 min. Saposin was then added, and the mixture was incubated for another 2 min. The reconstitution reaction was prepared in a 1:230:30 molar ratio of protein, lipids, and saposin A. To help initiate reconstitution, the mixture was diluted ~10-fold with TBS buffer supplemented with 2 mM GABA and 100 µM S-nidradine. Bio-Beads SM-2 (Bio-Rad) were added at ~200 mg/mL to remove detergent. The reconstitution reaction was rotated overnight at 4 °C. The following morning, the Bio-beads were removed, and the sample was collected for size-exclusion chromatography.

Monoclonal antibody digestion and Fab purification

1F4 monoclonal antibody (mAb) against the $α_1$ subunit of the $GABA_A$ receptor (IgG2b, κ) was raised using standard methods (Monoclonal Core, Vaccine and Gene Therapy Institute, Oregon Health & Science University). Fab fragments were purified through papain cleavage. For 2 h at 37 °C, 0.5 mg/mL of mAb was incubated with papain in a 1:30 ratio (w/w) in 50 mM $NaPO_4$, pH 7.0, 1 mM EDTA, and 10 mM cysteine. The reaction was quenched by incubation with 30 mM iodoacetamide

at 25 °C for 10 min. Fab was purified through anion exchange chromatography using a HiTrap Q HP (GE Healthcare) column in 10 mM Tris, pH 8.0, with a NaCl gradient elution.

Cryo-EM sample preparation

The reconstituted receptors were mixed with 1F4 Fab in a 3:1 (w/w) ratio and incubated on ice for 15 min. The sample was concentrated to 0.5–1 mL and injected into a Superose 6 Increase 10/300 GL column (GE Healthcare), which had previously been equilibrated with TBS buffer supplemented with 2 mM GABA and 100 μM S-nidradine. Peak fractions were analyzed by fluorescence-detection size-exclusion chromatography, using tryptophan fluorescence. Target fractions were pooled and concentrated to ~2 mg/mL, then another 100 μM of S-nidradine was spiked into a final concentration of 200 μM. The sample was supplemented with 0.5 mM fluorinated Fos-Choline-8 (Anatrace) to induce random orientations immediately prior to freezing grids. Copper R2/1 200 mesh 2 nm continuous carbon grids (Quantifoil) were glow-discharged (PELCO easiGlow) for 30 s at 10 mA before addition of 3 μL of sample, followed by plunge-freezing in liquid ethane using a Vitrobot Mark IV (FEI). The grids were blotted for 3 s with a blot force of −15 at 100% humidity and 4 °C.

Cryo-EM data collection and processing

Cryo-EM data were collected at the University of California, San Diego Cryo-EM facility for 24 h on a 300 kV Titan Krios Microscope (FEI) equipped with a Falcon 4 direct electron detector and Selectris X energy filter. The total exposure was 50 e^{-} $Å^{-2}$, and the defocus range was set to −1.2 to −2.0 μm. The dataset was processed using CryoSPARC v4.6.2 and v.4.7. The images were motion and gain corrected using patch motion correction. Patch CTF was used for contrast transfer function estimation. Particles were selected, and 2× Fourier binned before three rounds of 2D classification. The selected particles were then re-extracted at full size and were then aligned with non-uniform refinement. Two focused 3D classification jobs were run with focus masks on the two β-α TMD interfaces. Classes with well-ordered TMDs were combined and duplicates removed. These particles were then aligned through another non-uniform refinement. This resulted in the final unsharpened map at a resolution of 2.9 Å, which was further sharpened through a DeepEMhancer job.

Model building, refinement, and validation

An initial model was built for the S-nidradine structure using ModelAngelo[85]. This model was then docked into the S-nidradine experimental map and was manually adjusted in Coot[86], with the $GABA_A$ receptor in complex with 1F4 fab, GABA, and etomidate (PDB ID: 6X3V) as reference. The model was subjected to global real-space and B-factor refinement with stereochemistry restraints in Phenix[87]. Geometry restraints for S-nidradine were generated using the Grade Web Server (Smart, O.S., Sharff A., Holstein, J., Womack, T.O., Flensburg, C., Keller, P., Paciorek, W., Vonrhein, C. and Bricogne G. (2021) Grade2 version 1.7.0. Cambridge, UK: Global Phasing Ltd). Model quality was checked with Phenix and Molprobity[88]. Sequences for sequence alignments were downloaded from the UniProt database, and alignments were made with Clustal Omega[89]. Hole2 was used to generate pore radius profiles[90]. UCSF ChimeraX[91] was used to generate structural figures. Densities consistent with some phospholipids were present in the unsharpened cryo-EM density map. While these densities were not particularly strong, we built them into the model based on consistency with earlier models[92].

Electrophysiology of the $GABA_A$ receptor

Whole-cell voltage-clamp electrophysiology recordings were collected from adherent HEK293S GnTI^{-} cells. Recordings for WT α1β2γ2 receptors were collected from stable cell lines created with a Sleeping Beauty transposon system. For the mutant α1β2γ2 receptors, adherent HEK293S GnTI^{-} cells were transiently transfected using Lipofectamine 2000 (Invitrogen) with a tri-cistronic pEZT construct encoding the mutant receptors and a GFP protein in pEZT for selection. For the α4β2γ2, α5β2γ2, and α4β2δ receptors, adherent HEK293S GnTI^{-} cells were transiently transfected using Lipofectamine2000 (Invitrogen) with pEZT-based plasmids encoding each subunit along with GFP in pEZT. Full-length subunits were transfected in a 1 α:1 β2:5 γ2/δ ratio. After transfection or protein expression induction, the cells were incubated at 30 °C for 48–96 h. On the day of recording, cells were plated onto 35 mm dishes and washed with bath solution (140 mM NaCl, 4 mM KCl, 2 mM $CaCl_2$, 1 mM $MgCl_2$, 5 mM glucose, and 10 mM HEPES, pH 7.4). Borosilicate pipettes were pulled and polished to an initial resistance of 2.5–3.5 MΩ. Pipettes were filled with pipette solution (110 mM CsF, 10 mM CsCl, 10 mM NaCl, 10 mM HEPES, pH 7.2, and 10 mM EGTA). Cells were clamped at −75 mV. Whole cell currents were recorded with an Axopatch 200B amplifier, sampled at 10 kHz, and low-pass filtered at 2 kHz using a Digidata 1440A (Molecular Devices), and analyzed with Clampfit 11 software (Molecular Devices). Solutions were exchanged using a gravity-driven RSC-200 rapid solution changer (Bio-Logic). Ligand solutions were prepared in the bath solution.

Statistical analysis of the $GABA_A$ receptor electrophysiology data

Statistical analysis was performed using GraphPad Prism 10.6.0 software (GraphPad Software, Inc., La Jolla, CA). Data are expressed as mean values ± standard error of the mean of at least four recordings from independent cells. Two-tailed Welch's *t*-tests were used. A *p*-value of <0.05 was considered statistically significant.

General procedure for synthesis of oxazolecarboxamides and isoxazolecarboxamides, and spectral data of synthesized intermediates are shown in the Supplementary Information.

Reporting summary

Further information on research design is available in the Nature Portfolio Reporting Summary linked to this article.

Data availability

The cryo-EM map has been deposited in the Electron Microscopy Data Bank (EMDB) under accession code EMD-73211. The atomic coordinates have been deposited in the Protein Data Bank (PDB) under accession code 9YNN. Source data are provided as a Source Data file. Full list of compounds screened and phenoscore plotting script are provided as Supplementary Data File 1 and File 2, respectively, accompanying this article. The complete time-series behavioral dataset generated during the phenotypic screen is publicly available in Parquet format through Zenodo (https://doi.org/10.5281/zenodo.22312888). Source data are provided with this paper.

References

1. McQueen, K. A. K. Anesthesia and the global burden of surgical disease. *Int. Anesthesiol. Clin.* **48**, 91–107 (2010).
2. Gu, W.-J., Wang, F., Tang, L. & Liu, J.-C. Single-dose etomidate does not increase mortality in patients with sepsis: a systematic review and meta-analysis of randomized controlled trials and observational studies. *Chest* **147**, 335–346 (2015).
3. Bruder, E. A., Ball, I. M., Ridi, S., Pickett, W. & Hohl, C. Single induction dose of etomidate versus other induction agents for endotracheal intubation in critically ill patients. *Cochrane Database Syst. Rev.* **1**, CD010225 (2015).
4. Kim, J. J. et al. Shared structural mechanisms of general anaesthetics and benzodiazepines. *Nature* **585**, 303–308 (2020).
5. Abdulzahir, A. et al. Changes in memory, sedation, and receptor kinetics imparted by the β2-N265M and β3-N265M GABAA receptor point mutations. *Int. J. Mol. Sci.* **24**, 5637 (2023).

6. Franks, N. P. Molecular targets underlying general anaesthesia. *Br. J. Pharmacol.* **147**, S72–S81 (2006).
7. Olsen, R. W. & Sieghart, W. GABA A receptors: subtypes provide diversity of function and pharmacology. *Neuropharmacology* **56**, 141–148 (2009).
8. Olsen, R. W. & Sieghart, W. International Union of Pharmacology. LXX. Subtypes of gamma-aminobutyric acid(A) receptors: classification on the basis of subunit composition, pharmacology, and function. Update. *Pharmacol. Rev.* **60**, 243–260 (2008).
9. Zhou, J. et al. Resolving native GABAA receptor structures from the human brain. *Nature* **638**, 562–568 (2025).
10. Frölich, M. A. et al. The effect of propofol on thermal pain perception. *Anesth. Analg.* **100**, 481–486 (2005).
11. Fassoulaki, A. Is propofol an analgesic? *Eur. J. Anaesthesiol.* **28**, 481–482 (2011).
12. Santa, C. et al. Association of intraoperative opioid administration with postoperative pain and opioid use. *JAMA Surg.* **158**, 854–864 (2023).
13. Kokel, D. et al. Rapid behavior-based identification of neuroactive small molecules in the zebrafish. *Nat. Chem. Biol.* **6**, 231–237 (2010).
14. McCarroll, M. N., Gendelev, L., Keiser, M. J. & Kokel, D. Leveraging large-scale behavioral profiling in zebrafish to explore neuroactive polypharmacology. *ACS Chem. Biol.* **11**, 842–849 (2016).
15. Yang, X. et al. High throughput screening in larval zebrafish identifies novel potent sedative-hypnotics. *Anesthesiology* **129**, 459–476 (2018).
16. Plasencia, D. M., Rodgers, L. H., Knighton, A. R., Eckenhoff, R. G. & White, E. R. Antagonism of propofol anesthesia by alkylfluorobenzene derivatives. *Sci. Rep.* **14**, 15943 (2024).
17. McCarroll, M. N. et al. Zebrafish behavioural profiling identifies GABA and serotonin receptor ligands related to sedation and paradoxical excitation. *Nat. Commun.* **10**, 4078 (2019).
18. Kalueff, A. V., Stewart, A. M. & Gerlai, R. Zebrafish as an emerging model for studying complex brain disorders. *Trends Pharmacol. Sci.* **35**, 63–75 (2014).
19. Baraban, S. C., Dinday, M. T. & Hortopan, G. A. Drug screening in Scn1a zebrafish mutant identifies clemizole as a potential Dravet syndrome treatment. *Nat. Commun.* **4**, 2410 (2013).
20. Tolete, P. et al. Lorcaserin therapy for severe epilepsy of childhood onset. *Neurology* **91**, 837–839 (2018).
21. Kitcher, S. R. et al. ORC-13661 protects sensory hair cells from aminoglycoside and cisplatin ototoxicity. *JCI Insight* **4**, e126764 (2019).
22. Monesson-Olson, B. et al. Expression of the eight GABAA receptor α subunits in the developing zebrafish central nervous system. *PLoS ONE* **13**, e0196083 (2018).
23. Bąchor, Mączyński, U. & Sochacka-Ćwikła, M. A. Therapeutic potential of isoxazole-(iso)oxazole hybrids: three decades of research. *Int. J. Mol. Sci.* **26**, 7082 (2025).
24. Fleming, A., Diekmann, H. & Goldsmith, P. Functional characterisation of the maturation of the blood–brain barrier in larval zebrafish. *PLoS ONE* **8**, e77548 (2013).
25. Petersen, B. D., Bertoncello, K. T. & Bonan, C. D. Standardizing zebrafish behavioral paradigms across life stages: an effort towards translational pharmacology. *Front. Pharmacol.* **13**, 833227 (2022).
26. Virtanen, M. A., Uvarov, P., Mavrovic, M., Poncer, J. C. & Kaila, K. The multifaceted roles of KCC2 in cortical development. *Trends Neurosci.* **44**, 378–392 (2021).
27. Dixon, W. J. The up-and-down method for small samples. *J. Am. Stat. Assoc.* **60**, 967–978 (1965).
28. Chen, Y. et al. A simple and sensitive HPLC-MS/MS method for the simultaneous quantitative analysis and pharmacokinetic comparison of four imidazole-derived GABA receptor agonists: etomidate, metomidate, propoxate, and isopropoxate in mouse blood. *Biomed. Chromatogr. BMC* **39**, e70226 (2025).
29. McCarroll, M. N. et al. A multimodal, in vivo approach for assessing structurally and phenotypically related neuroactive molecules. *ACS Chem. Neurosci.* **15**, 4171–4184 (2024).
30. Ruesch, D., Neumann, E., Wulf, H. & Forman, S. A. An allosteric coagonist model for propofol effects on α1β2γ2L γ-aminobutyric acid type A receptors. *Anesthesiology* **116**, 47–55 (2012).
31. Ghit, A., Assal, D., Al-Shami, A. S. & Hussein, D. E. E. GABAA receptors: structure, function, pharmacology, and related disorders. *J. Genet. Eng. Biotechnol.* **19**, 123 (2021).
32. Brickley, S. G. & Mody, I. Extrasynaptic GABA(A) receptors: their function in the CNS and implications for disease. *Neuron* **73**, 23–34 (2012).
33. Kim, J. J. & Hibbs, R. E. Direct structural insights into GABAA receptor pharmacology. *Trends Biochem. Sci.* **46**, 502–517 (2021).
34. Deady, J. E., Koblin, D. D., Eger, E. I., Heavner, J. E. & D'Aoust, B. Anesthetic potencies and the unitary theory of narcosis. *Anesth. Analg.* **60**, 380–384 (1981).
35. Andrews, D. T., Leslie, K., Sessler, D. I. & Bjorksten, A. R. The arterial blood propofol concentration preventing movement in 50% of healthy women after skin incision. *Anesth. Analg.* **85**, 414–419 (1997).
36. Leslie, K., Bjorksten, A. R., Ugoni, A. & Mitchell, P. Mild core hypothermia and anesthetic requirement for loss of responsiveness during propofol anesthesia for craniotomy. *Anesth. Analg.* **94**, 1298–1303 (2002). table of contents.
37. Herd, D. W., Anderson, B. J., Keene, N. A. & Holford, N. H. G. Investigating the pharmacodynamics of ketamine in children. *Paediatr. Anaesth.* **18**, 36–42 (2008).
38. Weinrich, J. A. P. et al. Paradoxical increases in anterior cingulate cortex activity during nitrous oxide-induced analgesia reveal a signature of pain affect. *Pain* **166**, 2576–2587 (2025).
39. Besnard, J. et al. Automated design of ligands to polypharmacological profiles. *Nature* **492**, 215–220 (2012).
40. Ben-Ari, Y. The GABA excitatory/inhibitory developmental sequence: a personal journey. *Neuroscience* **279**, 187–219 (2014).
41. Mueller, T., Vernier, P. & Wullimann, M. F. A phylotypic stage in vertebrate brain development: GABA cell patterns in zebrafish compared with mouse. *J. Comp. Neurol.* **494**, 620–634 (2006).
42. Zhang, R., Wei, H., Xia, Y. & Du, J. Development of light response and GABAergic excitation-to-inhibition switch in zebrafish retinal ganglion cells. *J. Physiol.* **588**, 2557–2569 (2010).
43. Barnaby, W. et al. GABAA α subunit control of hyperactive behavior in developing zebrafish. *Genetics* **220**, iyac011 (2022).
44. Roussel, Y., Paradis, M., Gaudreau, S. F., Lindsey, B. W. & Bui, T. V. Spatiotemporal transition in the role of synaptic inhibition to the tail beat rhythm of developing larval zebrafish. *eNeuro* **7**, ENEURO.0508-18.2020 (2020).
45. Guarin, M. et al. Pharmacokinetics in zebrafish embryos (ZFE) following immersion and intrayolk administration: a fluorescence-based analysis. *Pharmaceuticals* **14**, 576 (2021).
46. Eliceiri, B. P., Gonzalez, A. M. & Baird, A. Zebrafish model of the blood-brain barrier: morphological and permeability studies. *Methods Mol. Biol. Clifton NJ* **686**, 371–378 (2011).
47. Martis, G. J. & Gaonkar, S. L. Advances in isoxazole chemistry and their role in drug discovery. *RSC Adv.* **15**, 8213–8243 (2025).
48. Li, S. et al. Oxazole and isoxazole-containing pharmaceuticals: targets, pharmacological activities, and their SAR studies. *RSC Med. Chem.* **16**, 1879–1890 (2025).
49. Agrawal, N. & Mishra, P. The synthetic and therapeutic expedition of isoxazole and its analogs. *Med. Chem. Res.* **27**, 1309–1344 (2018).

50. Das, S. & Chanda, K. An overview of metal-free synthetic routes to isoxazoles: the privileged scaffold. *RSC Adv.* **11**, 32680–32705 (2021).
51. Pairas, G. N., Perperopoulou, F., Tsoungas, P. G. & Varvounis, G. The isoxazole ring and its N-oxide: a privileged core structure in neuropsychiatric therapeutics. *ChemMedChem* **12**, 408–419 (2017).
52. Eger, E. I. Age, minimum alveolar anesthetic concentration, and minimum alveolar anesthetic concentration-awake. *Anesth. Analg.* **93**, 947–953 (2001).
53. Katoh, T. & Ikeda, K. The effects of fentanyl on sevoflurane requirements for loss of consciousness and skin incision. *Anesthesiology* **88**, 18–24 (1998).
54. Dunnet, J. M., Prys-Roberts, C., Holland, D. E. & Browne, B. L. Propofol infusion and the suppression of consciousness: dose requirements to induce loss of consciousness and to suppress response to noxious and non-noxious stimuli. *Br. J. Anaesth.* **72**, 29–34 (1994).
55. von Dincklage, F., Send, K., Hackbarth, M., Rehberg, B. & Baars, J. H. Comparison of the nociceptive flexion reflex threshold and the bispectral index as monitors of movement responses to noxious stimuli under propofol mono-anaesthesia. *Br. J. Anaesth.* **102**, 244–250 (2009).
56. Aho, A. J., Yli-Hankala, A., Lyytikäinen, L.-P. & Jäntti, V. Facial muscle activity, Response Entropy, and State Entropy indices during noxious stimuli in propofol-nitrous oxide or propofol-nitrous oxide-remifentanil anaesthesia without neuromuscular block. *Br. J. Anaesth.* **102**, 227–233 (2009).
57. Zheng, H., Zhu, Y., Chen, K. & Shen, X. The effect of etomidate or propofol on brainstem function during anesthesia induction: a bispectral index-guided study. *Drug Des. Dev. Ther.* **13**, 1941–1946 (2019).
58. Homma, Y. et al. A mini-review of procedural sedation and analgesia in the emergency department. *Acute Med. Surg.* **7**, e574 (2020).
59. Jaeger, J. M., Rice, D. C. & Albright-Trainer, B. Battlefield medicine: anesthesia and critical care in the combat zone. *Anesthesiol. Clin.* **39**, 321–336 (2021).
60. Reynolds, D. S. et al. Sedation and anesthesia mediated by distinct GABA(A) receptor isoforms. *J. Neurosci. Off. J. Soc. Neurosci.* **23**, 8608–8617 (2003).
61. Jurd, R. et al. General anesthetic actions in vivo strongly attenuated by a point mutation in the GABA(A) receptor beta3 subunit. *FASEB J. Off. Publ. Fed. Am. Soc. Exp. Biol.* **17**, 250–252 (2003).
62. Baron, M. & Devor, M. From molecule to oblivion: dedicated brain circuitry underlies anesthetic loss of consciousness permitting pain-free surgery. *Front. Mol. Neurosci.* **16**, 1197304 (2023).
63. Antognini, J. F. & Carstens, E. Macroscopic sites of anesthetic action: brain versus spinal cord. *Toxicol. Lett* **100–101**, 51–58 (1998).
64. Kungys, G., Kim, J., Jinks, S. L., Atherley, R. J. & Antognini, J. F. Propofol produces immobility via action in the ventral horn of the spinal cord by a GABAergic mechanism. *Anesth. Analg.* **108**, 1531–1537 (2009).
65. Green, C. J., Knight, J., Precious, S. & Simpkin, S. Ketamine alone and combined with diazepam or xylazine in laboratory animals: a 10 year experience. *Lab. Anim.* **15**, 163–170 (1981).
66. Tomi, K. et al. Alterations in pain threshold and psychomotor response associated with subanaesthetic concentrations of inhalation anaesthetics in humans. *Br. J. Anaesth.* **70**, 684–686 (1993).
67. Janiszewski, D. J. et al. The effects of subanesthetic concentrations of sevoflurane and nitrous oxide, alone and in combination, on analgesia, mood, and psychomotor performance in healthy volunteers. *Anesth. Analg.* **88**, 1149–1154 (1999).
68. Petrenko, A. B. et al. Effects of ketamine on acute somatic nociception in wild-type and N-methyl-D-aspartate (NMDA) receptor epsilon1 subunit knockout mice. *Neuropharmacology* **50**, 741–747 (2006).
69. Hammo, A., Wisser, S. & Cichon, J. Single-dose psilocybin rapidly and sustainably relieves allodynia and anxiodepressive-like behaviors in mouse models of chronic pain. *Nat. Neurosci.* **28**, 2285–2295 (2025).
70. Gregory, N. S. et al. No evidence of immediate or persistent analgesic effect from a single dose of psilocybin in three mouse models of pain. *Nat. Commun.* **17**, 1916 (2026).
71. Zhu, X.-N. et al. Propofol exerts anti-anhedonia effects via inhibiting the dopamine transporter. *Neuron* **111**, 1626–1636.e6 (2023).
72. Westerfield, M. *The Zebrafish Book. A Guide for the Laboratory Use of Zebrafish (Danio Rerio)* (University of Oregon Press, 2015).
73. Bruni, G. et al. Zebrafish behavioral profiling identifies multitarget antipsychotic-like compounds. *Nat. Chem. Biol.* **12**, 559–566 (2016).
74. Myers-Turnbull, D. et al. *Simultaneous Classification of Neuroactive Compounds in Zebrafish*. https://doi.org/10.1101/2020.01.01.891432 (2020).
75. Gendelev, L. et al. Deep phenotypic profiling of neuroactive drugs in larval zebrafish. *Nat. Commun.* **15**, 9955 (2024).
76. Fink, E. A. et al. Structure-based discovery of nonopioid analgesics acting through the α2A-adrenergic receptor. *Science* **377**, eabn7065 (2022).
77. Yeh, C.-M., Glöck, M. & Ryu, S. An optimized whole-body cortisol quantification method for assessing stress levels in larval zebrafish. *PLoS ONE* **8**, e79406 (2013).
78. Gupta, A. R. et al. Development of a viable tissue acquisition laboratory core: a generalizable partnership model to advance groundbreaking human biology. *Transplantation* **110**, e1361–e1363 (2026).
79. Kelly, Y. M. et al. Effects of multi-stage procurement on the viability and function of human donor parathyroid glands. *J. Surg. Res.* **276**, 404–415 (2022).
80. Zhu, S. et al. Structure of a human synaptic GABAA receptor. *Nature* **559**, 67–72 (2018).
81. Jansen, M., Bali, M. & Akabas, M. H. Modular design of Cys-loop ligand-gated ion channels: functional 5-HT3 and GABA rho1 receptors lacking the large cytoplasmic M3M4 loop. *J. Gen. Physiol.* **131**, 137–146 (2008).
82. Kowarz, E., Löscher, D. & Marschalek, R. Optimized Sleeping Beauty transposons rapidly generate stable transgenic cell lines. *Biotechnol. J.* **10**, 647–653 (2015).
83. Chojnacka, W., Teng, J., Kim, J. J., Jensen, A. A. & Hibbs, R. E. Structural insights into GABAA receptor potentiation by Quaalude. *Nat. Commun.* **15**, 5244 (2024).
84. Zhu, S. et al. Structural and dynamic mechanisms of GABAA receptor modulators with opposing activities. *Nat. Commun.* **13**, 4582 (2022).
85. Jamali, K. et al. Automated model building and protein identification in cryo-EM maps. *Nature* **628**, 450–457 (2024).
86. Emsley, P. & Cowtan, K. Coot: model-building tools for molecular graphics. *Acta Crystallogr. D Biol. Crystallogr.* **60**, 2126–2132 (2004).
87. Adams, P. D. et al. PHENIX: a comprehensive Python-based system for macromolecular structure solution. *Acta Crystallogr. D Biol. Crystallogr.* **66**, 213–221 (2010).
88. Chen, V. B. et al. MolProbity: all-atom structure validation for macromolecular crystallography. *Acta Crystallogr. D Biol. Crystallogr.* **66**, 12–21 (2010).
89. Sievers, F. & Higgins, D. G. Clustal omega. *Curr. Protoc. Bioinform.* **48**, 3.13.1–3.13.16 (2014).
90. Smart, O. S., Neduvelil, J. G., Wang, X., Wallace, B. A. & Sansom, M. S. HOLE: a program for the analysis of the pore

dimensions of ion channel structural models. *J. Mol. Graph.* **14**, 354–360, 376 (1996).
91. Pettersen, E. F. et al. UCSF ChimeraX: structure visualization for researchers, educators, and developers. *Protein Sci. Publ. Protein Soc.* **30**, 70–82 (2021).
92. Legesse, D. H. et al. Structural insights into opposing actions of neurosteroids on GABAA receptors. *Nat. Commun.* **14**, 5091 (2023).

Acknowledgements

We thank Louie Ramos for exceptional animal care and husbandry. ELISA plate reader analysis was performed at the UCSF Center for Advanced Technology, supported by UCSF PBBR, RRP IMIA, and NIH 1S10OD028511-01 grants. The authors acknowledge the facilities of the UC San Diego cryo-EM facility, part of the Goeddel Family Technology Sandbox, along with the scientific and technical assistance of facility staff members Dr. Mariusz Matyszewski and Dr. Inga Kuschnerus. We thank Kaity Hammerstein for assistance with zebrafish illustrations used in the main figures. Ki determinations and receptor binding profiles were generously provided by the National Institute of Mental Health's Psychoactive Drug Screening Program, Contract # 75N95023C00021 (NIMH PDSP). The NIMH PDSP is Directed by Bryan L. Roth, M.D., Ph.D., at the University of North Carolina at Chapel Hill and by Project Officer Jamie Driscoll at NIMH, Bethesda, MD, USA.

Author contributions

Conceptualization: M.N.N., D.K., J.K.S., J.A.P.W.; Methodology M.N.M., J.A.P.W., R.E.H., A.H.M., M.L., and Jf.T.; Software: M.N.M., D.M.T., C.H., J.A.P.W., R.K.; Formal Analysis, M.N.M., A.H.M., Jf.T., J.A.P.W., and R.K.; Investigation: M.N.M, J.A.P.W., X.G., A.D., A.H.M., E.S., Jf.T., J.C.T., L.X.P., M.J.L., C.A., A.C., R.D.L., R.Z., M.J, K.B., S.R.R., J.D., A.A., I.A., T.G., S.A.R., and J.K.; Resources: M.N.M, D.K., J.K.S., R.E.H, I.V., B.P.B., and A.I.B.; Data curation: M.N.M, D.M.T., C.H., A.H.M., and Jf.T.; Writing-original draft: M.N.M., J.A.P.W., and A.H.M.; Writing-reviewing and editing: M.N.M., R.E.H., J.A.P.W., M.B., A.I.B., A.H.M., and J.K.S.; Visualization: M.N.M., J.A.P.W., A.H.M., and Jf.T.; Supervision: M.N.M., R.E.H., D.K., A.I.B., B.P.B., I.V., B.K.S., and J.K.S.; Project administration: M.N.M., A.I.B., R.E.H., and J.K.S.; Funding acquisition, M.N.M, D.K., A.I.B., B.K.S., B.P.B., I.V., M.B., R.E.H., and J.K.S.

Funding

This work was supported by the Defense Advanced Research Projects Agency (DARPA) grant: W911NF-24-2-0109 (M.N.M., J.K.S., A.I.B., R.E.H., B.K.S., and M.P.B.) and the US National Institutes of Health (NIH) grants: DP1DA058350 (M.N.M.), AI123400-03 (J.K.S.), R01AA022583 (D.K.), F31NS145564 and T32GM007752 (A.H.M.), and R01DA047325 (R.E.H.). This work was also supported by the Chan Zuckerberg Initiative (J.K.S.), an advised fund of the Silicon Valley Community Foundation, and Ono Pharmaceutical (J.K.S.).

Competing interests

The authors declare the following competing interests: The University of California, San Francisco and the Chan Zuckerberg Biohub are applicants on a pending U.S. National Phase Patent Application (No. 19/513,062) related to the identification and use of nidradine and related compounds as anesthetic and analgesic agents described in this work. M.N.M., J.A.P.W., D.K., A.I.B., and J.K.S. are named as co-inventors. The remaining authors declare no competing interests.

Additional information

Supplementary information The online version contains supplementary material available at https://doi.org/10.1038/s41467-026-79384-x.

Correspondence and requests for materials should be addressed to Matthew N. McCarroll, Ryan E. Hibbs, Allan I. Basbaum or Jason K. Sello.

Peer review information *Nature Communications* thanks Mitra Heshmati, Paul S Miller and the other anonymous reviewer(s) for their contribution to the peer review of this work. A peer review file is available.

Reprints and permissions information is available at http://www.nature.com/reprints

Publisher's note Springer Nature remains neutral with regard to jurisdictional claims in published maps and institutional affiliations.

Open Access This article is licensed under a Creative Commons Attribution 4.0 International License, which permits use, sharing, adaptation, distribution and reproduction in any medium or format, as long as you give appropriate credit to the original author(s) and the source, provide a link to the Creative Commons licence, and indicate if changes were made. The images or other third party material in this article are included in the article's Creative Commons licence, unless indicated otherwise in a credit line to the material. If material is not included in the article's Creative Commons licence and your intended use is not permitted by statutory regulation or exceeds the permitted use, you will need to obtain permission directly from the copyright holder. To view a copy of this licence, visit http://creativecommons.org/licenses/by/4.0/.

© The Author(s) 2026

This Article in Press is shared early to give you faster access to new research. It is citable and carries a permanent DOI. The final edited version will replace it automatically.